

What drives the lifecycle of tropical anvil clouds?

Blaž Gasparini¹, Peter N. Blossey¹, Dennis L. Hartmann¹, Guangxing Lin²,
Jiwen Fan²

¹University of Washington, Seattle, Washington, USA

²Pacific Northwest National Laboratory, Richland, Washington, USA

Key Points:

- Both radiative and latent heating within anvil clouds strongly influence the cloud radiative effect at the top of the atmosphere
- Latent and radiative heating drive turbulence and organized circulations within the anvil cloud structure
- Radiative heating dominates near the top of the cloud, while latent heating dominates near the base of the cloud

Corresponding author: Blaž Gasparini, blazg@uw.edu

13 **Abstract**

14 The net radiative effects of tropical clouds are determined by the evolution of thick, freshly
15 detrained anvil clouds into thin anvil clouds. Thick anvil clouds reduce Earth's energy
16 balance and cool the climate, while thin anvil clouds warm the climate. To determine
17 role of these clouds in climate change we need to understand how interactions of their
18 micro- and microphysical properties control their radiative properties. We explore anvil
19 cloud evolution using a cloud resolving model in three simulation setups of increasing
20 complexity to disentangle the impacts of the various components of diabatic heating and
21 their interaction with cloud-scale motions.

22 The first phase of evolution and rapid cloud spreading is dominated by latent heat-
23 ing within convective updrafts. After the convective detrainment stops, most of the spread-
24 ing and thinning of the anvil cloud is driven by cloud radiative processes and latent heat-
25 ing. The combination of radiative cooling at cloud top, latent cooling due to sublima-
26 tion at cloud base, latent heating due to deposition and radiative heating in between leads
27 to a sandwich-like, cooling-heating-cooling structure. The heating sandwich promotes
28 the development of two within-anvil convective layers and a double cell circulation, dom-
29 inated by strong outflow at 12 km altitude with inflow above and below.

30 Our study reveals how small-scale processes including convective, microphysical pro-
31 cesses, latent and radiative heating interact within the anvil cloud system. The absence
32 or a different representation of only one component results in a significantly different cloud
33 evolution with large impacts on cloud radiative effects.

Abstract

PLAIN LANGUAGE SUMMARY

Clouds have a large influence on climate. Thick clouds reflect part of the solar (or shortwave) radiation back to space and therefore cool the climate. On the other hand, wispy and thin high clouds do not reflect much of solar radiation. They form high in the atmosphere at cold temperatures and therefore keep part of the terrestrial (or longwave) radiation within the atmosphere. They warm the climate, similarly to greenhouse gasses.

The evolution of thunderstorm clouds is of particular interest as it involves a transition from the thick clouds that cool the climate to the thin high clouds that warm the climate. We study small-scale processes that drive this transition and their delicate balance and interactions. Tiny differences in how ice crystals form, grow, shrink, or interact with solar or terrestrial radiation can lead to large differences in the climatic role of thunderstorm clouds.

Such processes are currently not represented in models we use for climate projections. Our findings may ultimately lead to improvements in the representation of thunderstorm cloud lifecycles in climate models and therefore increase the trust in projections of future climate.

1 Introduction

In the tropical regions of prevalent ascent, clouds strongly modulate both the shortwave (SW) and longwave (LW) radiative fluxes, leading to large SW and LW cloud radiative effects (CRE) (Ramanathan et al., 1989). High ice clouds cover a large fraction of the tropics (Sassen et al., 2009; Martins et al., 2011). While the thickest precipitating high clouds have both large SW and large LW CRE, they are not the most dominant cloud type radiatively due to their short lifetime and limited spatial coverage. They fundamentally control the tropical CRE, however, through detrainment of large quantities of ice crystals (ICs). These crystals form anvil clouds, which spread over surface areas much larger than the deep convective cores from which they originate (Protopapadaki et al., 2017). Their combination of a moderate CRE and frequent occurrence makes detrained ice clouds the radiatively most important high cloud type in the tropics (Berry & Mace, 2014; Hartmann & Berry, 2017). Moreover, previous observational and modelling studies have shown that at least 50% of all ubiquitous tropical thin cirrus directly originate from deep convective sources (Massie et al., 2002; Luo & Rossow, 2004; Riihimaki et al., 2012; Gehlot & Quaas, 2012; Gasparini et al., 2018).

The lifecycle of anvil clouds is controlled by a number of processes including radiative heating due to in-atmospheric cloud radiative effects (ACRE), latent heating, microphysical processes like IC nucleation and growth, IC sedimentation, mixing of environmental air across cloud interfaces, turbulence, and cloud-scale circulations. However, it is still not fully understood what are the main drivers of anvil cloud extent, their microphysical, and radiative properties nor what controls the tropical CRE. Moreover, it is not clear whether the delicate balance between small-scale processes can change in a warmer climate, and what could be the climatic impacts of such a change.

Ackerman et al. (1988) were the first to quantify the radiative heating rates within tropical anvils based on in-situ aircraft data. The measured anvils were dominated by the LW warming effect, concentrated near cloud base, and LW cooling at the cloud top, that coincides with a minor SW warming effect. They hypothesized that the large heating gradients can lead to convective instability within an anvil. Their ideas were formalized in theoretical work by Lilly (1988) who proposed a two-stage model of the cirrus convective outflow. The initial outflow of air of nearly uniform buoyancy from the convective core flattens and stretches shortly after being injected into a stably stratified environmental air. The following stage is driven by differential radiative heating, forming a self-maintaining radiative-convective mixed layer within an anvil. The existence of within-

85 anvil convective motions was confirmed by numerous observational and modelling stud-
 86 ies (Jensen et al., 2009; Ferlay et al., 2014; Dobbie & Jonas, 2001; Durran et al., 2009;
 87 T. P. Dinh et al., 2010; Harrop & Hartmann, 2016). However, both Ackerman et al. (1988)
 88 and Lilly (1988) neglected the latent heating, which leads to strong heating by deposi-
 89 tion and freezing throughout most of the anvil, and cooling at and below cloud base due
 90 to sublimation, melting, and evaporation of precipitation (Houze, 1982; Starr & Cox, 1985;
 91 Lohmann & Roeckner, 1995; Schumacher et al., 2004; C. Liu et al., 2015). The anvil cloud
 92 extent and its lifetime were found to be sensitive to the IC size and number concentra-
 93 tion. Fan et al. (2010, 2013) showed how different specifications of cloud condensation
 94 nuclei and ice nucleating particles led to differing anvil cloud properties. Hartmann et
 95 al. (2018) found that ACRE promote the formation and maintenance of thin anvils with
 96 the help of two-dimensional cloud resolving model simulations. ACRE increase the longevity
 97 of thin anvils by microphysical cycling of water vapor and ICs within the in-cloud con-
 98 vective mixed layer. This ACRE-driven mechanism was crucial to achieve a balanced net
 99 CRE. Our study expands on that work by using three dimensional simulations allowing
 100 the cloud to evolve by spreading into its surrounding, cloud-free environment.

101 Garrett et al. (2005) describe a single case study of aircraft measurements of mi-
 102 crophysical and radiative properties of the first 3 hours of the anvil evolution. Their mea-
 103 surement showed the initial detrained mass was quickly separated into a thick anvil cloud,
 104 which detached from the convective core after 2 hours. Interestingly, above the anvil, a
 105 thin tropopause cirrus formed. The anvil gradually decayed, but the tropopause cirrus
 106 did not dissipate, likely due to the shielding effect of the (at least initially) optically thick
 107 underlying anvil (Hartmann, Holton, & Fu, 2001). Disagreements still exist about the
 108 radiative and microphysical importance of small ICs (Whiteway et al., 2004; Jensen et
 109 al., 2009; Protat et al., 2011), and the possibility of new nucleating events in the later
 110 stages of anvil evolution. A modelling study by Jensen et al. (2018) follows trajectories
 111 of ICs detrained from a midlatitude thunderstorm and simulates the first 3 hours of their
 112 microphysical evolution. Their results show at the importance of gravitational settling
 113 and depositional growth. However, due to the lack of radiative coupling, they do not ob-
 114 serve any convective overturning within the anvil cloud.

115 The parameterization of ice microphysics can significantly affect the simulated anvil
 116 cloud properties in the tropics. Powell et al. (2012) compared the observed West African
 117 anvil cloud properties with those simulated by 6 microphysical schemes in the WRF re-
 118 gional weather model (Skamarock et al., 2008). The results showed a large dependence
 119 on the specific microphysical scheme, while none of the schemes was able to represent
 120 the anvil properties within the range of the observations. Hartmann et al. (2018) found
 121 large differences in anvil cloud lifetime between the Thompson, Morrison, and P3 mi-
 122 crophysical schemes (Thompson et al., 2008; Morrison et al., 2005; Morrison & Milbrandt,
 123 2015), which modulated the impact of ACRE on the simulated cloud evolution.

124 A study by Schmidt and Garrett (2013) presents an analytic framework of the evo-
 125 lution of non-precipitating ice clouds of various thickness. Their thickest cloud, with ice
 126 water content (IWC) and extent similar to observed anvil clouds, forms two separate ra-
 127 diatively driven mixed-layers, one at cloud base, and the second one at cloud top. They
 128 show that the cloud initially spreads isentropically as a turbulent density current, tran-
 129 siting to laminar spreading and lofting motions once the cloud loses its turbulent behav-
 130 ior.

131 Previous studies focused only on one phase or one aspect of the anvil lifecycle, while
 132 we want to explore the main small-scale drivers over the whole lifecycle, from the thick
 133 deep convective cloud to the thin cirrus. Therefore we set up simulations of three increas-
 134 ing levels of complexity:

- 135 • a thick ice cloud in the middle of a cloud-free domain, initially in buoyant equi-
 136 librium with the environment;

- an isolated tropical deep convective system, in which we follow the cloud from the convective initiation from a warm, moist bubble until its decay;
- a longer, "climatological" simulation of radiative convective equilibrium (RCE), in which we statistically cluster the information over a large ensemble of convective events that maintain RCE.

Having simulations of differing complexity increases the robustness of the results and underlines the importance of small-scale processes in driving of the spreading and thinning of anvil clouds.

2 Modelling setup

We use System for Atmospheric Modelling (SAM) cloud resolving model (Khairoutdinov & Randall, 2003) version 6.10. The simulations use a 256 x 256 km domain with a horizontal resolution of 1 km and vertical resolution of 250 m in the upper troposphere, except for the RCE simulations (described in Section 2.3). The model top is at 27 km. The longer duration RCE simulations use a smaller, 128 x 128 km horizontal domain with the same vertical grid. SAM is a nonhydrostatic anelastic model with periodic lateral boundary conditions coupled with the RRTMG radiative transfer model (Mlawer et al., 1997; Iacono et al., 2008). Subgrid-scale motions are represented with a 1.5-order closure scheme that incorporates a simple Smagorinsky-type scheme. We coupled the model with the Predicted Particle Properties (P3) bulk microphysical scheme (Morrison & Milbrandt, 2015), version 2.8.2.4. P3 avoids the artificial separation of ice particles into its floating and precipitating parts; instead it uses four prognostic variables that track the mixing ratios of total ice mass, total ice number, rime mass and rime volume. Therefore, instead of specifying particle properties for several ice types (e.g. floating ice, snow, graupel), the scheme uses its 4 degrees of freedom to predict them. The scheme avoids artificial boundaries between particle types and avoids unphysical thresholds like the autoconversion radius of transition of ice to snow. P3 is therefore well suited for studies of transitions of deep, precipitating anvils, to thin, nonprecipitating cirrus; a situation, in which we expect numerous transitions between several categories of atmospheric ice particles. In order to allow the formation of clouds with number concentrations of ICs comparable to those observed in freshly detrained anvil clouds (Heymsfield, Krämer, Luebke, et al., 2017; Jensen et al., 2018), we increased the upper limit of IC number concentration from $0.5 \cdot 10^6$ to 10^7 kg^{-1} (about $2\text{-}5 \cdot 10^3$ L^{-1} at the anvil cloud altitudes). Simulations of the Dynamics of the MJO field campaign (Yoneyama et al., 2013) that used this increased upper limit on the IC number concentration showed good agreement with the observed radiative fluxes. The generalized effective IC size predicted by P3 is used in the computation of radiative fluxes.

For simplicity, diurnally-averaged insolation is used with a solar zenith angle of 42.89° and insolation (423.5 W m^{-2}) representative of the annual mean values in the tropics. The simulations are initialized without the presence of any mean winds and are not nudged. Sea surface temperature is fixed at 30°C . The simulations are described in Tab. 1.

2.1 Isolated cloud

We initialize the simulation with an optically thick high cloud (cloud optical depth (COD) of 120) of uniform IWC (0.3 g m^{-3}), which fits within the range of both in-situ and remote sensing observations of tropical anvil clouds (Garrett et al., 2005; Heymsfield, Krämer, Wood, et al., 2017; Heymsfield, Krämer, Luebke, et al., 2017). This simulation setup represents a freshly detrained anvil cloud, after most of the convective activity has ceased. The initial mean IC size is prescribed to follow observations by Van Diedenhoven et al. (2016), with an effective radius of 20 μm close to the cloud top, which increases linearly to reach 40 μm at the cloud base. The IC number concentration spans the range between 900 and 3600 L^{-1} , with the lowest concentrations at cloud base, and

187 concentration higher than 3000 L^{-1} above 10.5 km, which lies well within the range of
 188 in-situ observations (Jackson et al., 2015; Krämer et al., 2016; Heymsfield, Krämer, Lue-
 189 bke, et al., 2017). The cloud is initialized with random potential temperature pertur-
 190 bations of the order of 0.01°C , to help start the development of within-anvil motions.
 191 The cloud is 5 km thick with a top at 13 and base at 8 km altitude, which corresponds
 192 to the peak of the cloud cover in tropical convective regions (Protat et al., 2010; Hart-
 193 mann & Berry, 2017). The cloud is initially in buoyant equilibrium with the surround-
 194 ing environmental air. The cloud has an initial radius of 30 km and is centred in the mid-
 195 dle of the model domain, a 256 km square.

196 2.2 Isolated convection

197 We first decrease the specific humidity in the lowermost 3 km of the domain by 20%
 198 with respect to the typical tropical moisture profile to suppress convective plumes. The
 199 temperature profile is near the moist adiabat at all altitudes. Secondly, we initialize the
 200 simulation with a sinusoidal moisture perturbation with a peak of 5 g kg^{-1} , which de-
 201 cays both in the vertical and horizontal dimensions. The perturbation extends up to 3
 202 km in vertical, and 30 km in horizontal from its mid point. Such model initialization en-
 203 sures that convection starts first in the middle of the model domain and preserves a large
 204 degree of its azimuthal uniformity throughout the convective lifecycle, due the lack of
 205 any environmental winds.

We can decompose the total heating rate into the radiative (cloudy and clear-sky)
 and latent heating component with an additional residual term related mainly to unre-
 solved turbulent motions as:

$$\frac{dT}{dt} = Q_{rad,cld} + Q_{rad,cs} + Q_{latheat} + Q_{residual} \quad (1)$$

206 where T is temperature, t is time, and Q are the heating rates. We diagnose each of them
 207 directly from the model. We use azimuthal averaging, with the center of the domain (which
 208 is also the center of the cloud) being the center point of our cylindrical coordinate sys-
 209 tem.

The absence of geostrophic motions in the tropics results in weak horizontal tem-
 perature gradients (Charney, 1963). Therefore we use the weak temperature gradient
 approximation (e.g., Sobel and Bretherton (2000)) to derive the vertical velocities as-
 sociated with each of the heating terms using,

$$w \frac{\partial s}{\partial z} = Q c_p \quad (2)$$

where w is the azimuthally averaged vertical velocity and s is the dry static energy ($s = c_p T + gz$). We compute the residual vertical velocity as:

$$w_{residual} = w_{total} - w_{rad,cld} - w_{rad,cs} - w_{latheat} \quad (3)$$

Finally, we derive the total streamfunction from various heating sources (radiative,
 latent, and residual) by integrating the following equation in cylindrical coordinates over
 the radial dimension:

$$\frac{\partial \psi_i}{\partial r} = r w_i \quad (4)$$

$$\psi_i = \int_0^r r w_i dr \quad (5)$$

210 where r is the distance from the center of the domain and w_i represent the verti-
 211 cal velocities defined in equation (3).

2.3 Radiative convective equilibrium

The simulation is started with typical tropical temperature and moisture conditions, which quickly initiates convection. The simulation is run for 80 days, with a 2 hourly instantaneous output timestep for the 2D and 3D fields. For the purpose of the present analysis, we only consider 48 output timesteps from day 70-74 of the simulation, after the climate reached its equilibrium state. The model output is binned by increasing ice water path (IWP) values into 50 equispaced bins, each spanning 2% of all data points.

3 Observational data

We use the CALIPSO-CloudSat-CERES-MODIS (CCCM) dataset (Kato et al., 2011) for the years 2007-2010. The CCCM dataset combines CALIPSO lidar (Winker et al., 2010) and CloudSat radar (Stephens et al., 2008) cloud fraction collocated with MODIS IWP data and CERES radiative fluxes (Wielicki et al., 1996). We derive SW radiative fluxes from CERES, which are available only for daytime. To avoid problems at large solar zenith angles, we limit the data to points with zenith angle smaller than 70° , which restricts us to the afternoon overpass (1.30 pm) of the A-Train satellite constellation. We derive the albedo based on the incoming and outgoing SW fluxes at the top of the atmosphere (TOA). The diurnally-averaged reflected SW is computed by multiplying the albedo by the daily and annual averaged incoming radiation for the region of 423.5 W m^{-2} . We use data for the tropical western Pacific (TWP, $10^\circ\text{S} - 10^\circ\text{N}$ and $150^\circ - 170^\circ\text{E}$), a region dominated by deep convection year round. The albedo at the TOA and SW CRE are computed as

$$\text{albedo} = \frac{SW_{out}}{SW_{incoming}} \quad (6)$$

$$SW_{CRE} = -(\text{albedo} - \text{albedo}_{clear-sky}) * 423.5 \text{ W m}^{-2} \quad (7)$$

The LW CRE is computed as

$$LW_{CRE} = OLR_{clear} - OLR \quad (8)$$

where OLR is outgoing LW radiation at the TOA.

We bin the radiative fluxes and cloud fraction into 25 bins ordered by the percentiles of MODIS-derived IWP, each of them covering 4% of all considered points.

4 Results

Figure 1 shows the observed cloud fraction and its corresponding radiative effects binned by the respective IWP percentile values for the TWP. The high percentiles contain a fully cloud-covered troposphere and therefore represent deep convective towers, with both strong SW and LW CRE, where the SW component is the dominant one. The intermediately thick anvil clouds that spread from the convective core at 10-14 km altitude are responsible for a shift of net CRE from negative to positive close to the 75th IWP percentile. Such clouds contain IWP of 5 to 150 g m^{-2} and have COD between 1 and 6, and net CRE of about $+5$ to -25 W m^{-2} . The upper tropospheric cloud peak spreads towards higher altitudes when transiting to lower IWP values due to either the in-situ formation of new ice clouds or by lofting of anvil remains, as suggested by Hartmann and Berry (2017) and modeled by Hartmann et al. (2018). Remarkably, the net CRE shifts from values around -100 W m^{-2} for the highest percentiles, towards $+15$ to $+30 \text{ W m}^{-2}$ for the 40th to 70th percentiles. The crossover point in net CRE occurs near IWP of 100 g m^{-2} and COD of 4, roughly at the point where the cloud stops precipitating. The cloud columns maintain on average a net positive CRE even at lower percentiles, in which the tropical tropopause layer cirrus compete with infrequent, yet radiatively important boundary layer clouds. The average net CRE considering all selected clouds is $+0.6 \text{ W m}^{-2}$,

241 very close to being radiatively neutral. The radiative balance in the TWP is therefore
 242 controlled by a near perfect cancellation of the large SW and LW components when in-
 243 tegrated over all cloud types. Given the large SW and LW CRE, a small shift in the cloud
 244 distribution or its properties could result in large impacts on the radiative balance. This
 245 motivates us to study the details of the convective lifecycle, with a focus on the tran-
 246 sition between a freshly detrained, thick anvils, and aged, thin, anvil cloud remains.

247 4.1 Cloud radiative effect evolution

248 Figure 2 represents the time evolution of net CRE for the simulations of the iso-
 249 lated high cloud (a) and isolated convection (b). The former starts as a thick cloud dom-
 250 inated by its SW CRE. The cloud quickly starts spreading and thinning, increasing the
 251 thin cirrus fraction and its contribution to the overall radiative budget. The spreading
 252 is evident as both the domain averaged SW and LW CRE increase in the first 3 hours
 253 of the simulation, after which the SW effect decreases at a stronger pace than the LW
 254 CRE. This leads to a switch from a net negative to a net positive CRE. The cloud grad-
 255 ually thins until it becomes radiatively unimportant after 10 hours of simulation. The
 256 net CRE averaged over the whole lifecycle is slightly negative and about an order of mag-
 257 nitude smaller than the individual SW and LW CRE.

258 In Fig. 2b, isolated convection starts to develop quickly after the beginning of the
 259 simulation, leading to a small, 10-15 km broad convective core. The convection leads to
 260 a quickly-spreading cloud in the upper troposphere, whose diameter exceeds 100 km af-
 261 ter first 4 hours of the simulation. The cloud is still influenced by the convective detrain-
 262 ment in the first few hours, which generates a thick anvil cloud, dominated by SW CRE.
 263 The combination of a decreasing convective detrainment, stratiform precipitation, and
 264 spreading of the cloud leads to cloud thinning. The thin part of the cloud significantly
 265 modifies the outgoing LW radiative fluxes, despite being almost transparent to the in-
 266 coming SW radiation. The domain average CRE therefore transits from a net CRE neg-
 267 ative to a net CRE positive approximately 7 hours after the start of the simulation, reach-
 268 ing a peak between hour 11-12. While a thin anvil lingers in the atmosphere, new con-
 269 vective activity starts approximately at hour 13 of the simulation, marking the end of
 270 the studied convective lifecycle. The domain averaged integrated value of SW and LW
 271 CRE almost perfectly balance each other, yielding only a small, slightly positive net CRE,
 272 similarly to the near-cancellation of CRE observed in many tropical areas.

273 4.2 Isolated high cloud

274 We now examine in detail the evolution of the thick cylindrical ice cloud initial-
 275 ized in the middle of the domain.

276 4.2.1 Initial phase

277 The interactions of ICs and radiation instantaneously form a strong cooling of about
 278 -70 K day^{-1} at the cloud top (Fig. 3a,d). This LW cooling is partially compensated by
 279 the SW heating, which is able to penetrate further towards the interior of the cloud. The
 280 heated air below cloud top becomes positively buoyant and tries to rise above the sink-
 281 ing cool air at the cloud top. This helps establish in-cloud convective motions near cloud
 282 top within the first 15-30 min after the start of the simulation (Fig. S1). The convec-
 283 tive mixed layer is further intensified by the latent heating due to deposition and freez-
 284 ing in updrafts, and latent cooling by sublimation in downdrafts. However, the cloud top
 285 mixed layer forms even in experiments in which we turned off deposition (*NO DEPO*)
 286 and sublimation (*NO SUBI*, also refer to Tab. 1), but does not form in the *NO ACRE*
 287 simulation. The mixed layer grows in vertical from about 750 m to about 2 km in the
 288 first 2 h, after which it starts decaying. At that point circulations formed by diabatic
 289 heating take control of the cloud evolution (Fig 3 g,h,j,k and Fig. S1).

290 Similarly, the strong radiative heating at the cloud base combined with latent cool-
 291 ing by sublimation initiate a short-lived mixed layer just above cloud base 30 minutes
 292 after the beginning of the simulation (Figs. 3g and S2). A weak turbulent layer forms
 293 also near the peak of latent cooling just below the cloud base, which, however, cannot
 294 significantly influence the development of the overlying cloud. The *NO SUBI* experiment
 295 does not form mixed layers at cloud base, confirming the importance of sublimation for
 296 cloud base evolution. However, the absence of sublimation helps form a strong melting
 297 layer just below the 0°C isotherm, initiating small convective motions and a weak cir-
 298 culation pattern (Figs. S3 and 4c). The mixed layers at cloud base cannot fully develop
 299 due to the IC sedimentation and precipitation that inhibit the overturning motions. Both
 300 cloud top and cloud base mixed layers in the *NO SEDI* experiment continue to grow even
 301 beyond the first 2 hours of the simulation, eventually forming a single, self-sustained con-
 302 vective layer between 10 and 14 km altitude (Fig. S4).

303 The spreading of the cloud leads to a bowl-shape pattern (Fig. 3 b,c), consistent
 304 with the work of Schmidt and Garrett (2013). The cloud layer spreads along the isen-
 305 tropes, which are distorted by strong sources of diabatic heating and cooling (Fig. 3d-
 306 f). The bowl shape spreading still appears in *NO SEDI* (Fig. 4g) and is therefore not
 307 caused by sedimentation of ICs.

308 **4.2.2 Mature phase of development**

309 The mature phase starts with the decay of initial mixed layers and when the di-
 310 abatically driven circulations become fully developed (Fig. 3h,k). The initial radiatively
 311 driven heating structure now decreases in magnitude with the decreasing IWC of the cloud:
 312 sublimation forms a strong cooling anomaly, associated with a downdraft at and just be-
 313 low the wavy cloud base (Fig. 3e). A deposition driven heating anomaly in the center
 314 of the cloud sustains an updraft motion, which in turn leads to more vapor deposition
 315 (Fig. 3e). However, the cloud top is still dominated by radiative cooling, driving a down-
 316 draft motion which helps sustain a small mixed layer at the boundary of the radiative
 317 cooling and the latent-heating-driven updraft (Fig. 3h).

318 The diabatic heating not only drives vertical motions within cloud, but also sup-
 319 ports a circulation pattern as shown by Fig. 3j-l, which reaches its maximum around 4-
 320 5 hours after the beginning of the simulation. The circulation develops a two cell mo-
 321 tion:

- 322 • a radiatively driven circulation with a strong outflow at about 11-12 km and an
 323 equally strong inflow near the cloud top, between 13 and 14 km altitude (Fig. 3
 324 k).
- 325 • a latent heating driven circulation near cloud base, with an outflow below cloud
 326 base, and an inflow just above it.

327 The upper branch of the circulation leads to formation of a tropopause thin cir-
 328 rus (Fig. 3b,c). The origin of the cloud can be traced back to the radiatively driven in-
 329 flow and the associated convergence of air, which cuts off the uppermost cloud layers,
 330 and leads to an updraft just above cloud top (Fig. 3k). The updraft is further intensi-
 331 fied by depositional heating and new IC nucleation events. The tropopause cirrus can-
 332 not form in *NO ACRE* and *NO DEPO* simulations (Fig. 4b,d), but is still able to form
 333 weakly in *NO NUCI* (Fig. 4e). The tropopause cirrus therefore consists of both, pre-
 334 existing anvil cloud ICs and the newly nucleated ICs. The tropopause cirrus is long lived,
 335 as it is shielded from the terrestrial LW heating by the underlying anvil cloud. The cir-
 336 culation pattern moves together with the cloud edge (Fig. 3i,l), slowly decaying with the
 337 gradual sublimation and sedimentation of the cloud. Interestingly, a vigorous updraft
 338 continues to sustain the tropopause cirrus even when the anvil has substantially thinned
 339 (Fig. 3c,i). This later stage is characterized by vertically stratified pancake-like laminar

340 motions with only minimal vertical wind components, similarly to what was found by
 341 T. P. Dinh et al. (2010) for thin tropopause cirrus.

342 *4.2.3 Impact of the selected processes on the cloud radiative effects*

343 Most of the processes that we examine significantly influence the net CRE of the
 344 anvil cloud lifecycle. The control simulation yields a small negative net CRE over the
 345 course of its lifecycle (Fig. 2a). The simulation in which the ACRE were turned off (*NO*
 346 *ACRE*) yields a more negative CRE, as the cloud does not spread and thin due to the
 347 absence of radiatively-driven circulations and in-cloud convective motions (Fig. 4b). By
 348 limiting the nucleation of new ICs we also limit the formation of thin cirrus, leading to
 349 a significantly more negative net CRE (Fig. 4e). On the other hand, keeping the ICs aloft
 350 by not allowing them to sediment increases the net CRE which becomes significantly pos-
 351 itive (Fig. 4f). *NO SUBI* and *NO DEPO* simulations both yield a net negative integrated
 352 CRE over the course of 14 hours (Fig. 4c,d). Inhibiting sublimation results in the lack
 353 of particle removal and weaker circulations. Inhibiting deposition, on the other hand,
 354 drastically increases the production of new, radiatively very active small ICs, which have
 355 both a strong LW and SW CRE. Interestingly, the lack of deposition leads to an erosion
 356 of the internal parts of the cloud, which are normally dominated by depositional growth
 357 of ICs (Fig. 4d).

358 **4.3 Isolated convection**

359 The first deep convective activity develops at the location of the initial moist bub-
 360 ble. The moist air is buoyant and rises, forms clouds, and therefore gains more energy
 361 for its ascent due to the latent heating of condensation. About one hour from the be-
 362 ginning of the simulation, the convective cloud crosses the homogeneous freezing tem-
 363 perature for water, forming ICs, and releasing more latent heat to the environment, which
 364 pushes the updraft up to 18 km altitude (Figs. 5a,b and 6a,d,g). Despite developing a
 365 significant radiative heating of up to 20 K day^{-1} (Fig. 7c) it is the latent heating that
 366 dominates the initial cloud development. When the cloud reaches its maximum altitude,
 367 it starts to spread horizontally at velocities of $5\text{-}8 \text{ m s}^{-1}$ (Fig. 9). The convectively-driven
 368 latent heating also dictates the circulation pattern with a large updraft fed by the sur-
 369 face inflow, and detraining ICs between 12-15 km elevation (Figs. 7b and 8a,b). The large
 370 initial heating is a vigorous source of gravity waves (C. Bretherton, 1988), which signif-
 371 icantly perturb the instantaneous wind fields, while not influencing the mean winds.

372 The first phase ends after approximately 3 hours, when the cloud spreading veloc-
 373 ity temporarily slows down, before increasing again to about 2 m s^{-1} (Fig. 9). At this
 374 stage, when the cloud still contains a large IWC yielding an optical depth of 14 (Fig. 5b),
 375 the radiative driving becomes the dominant factor for the development of the cloud (Figs.
 376 7g, 8h). The spreading velocity of the *NO ACRE* experiment reaches values close to zero
 377 between 3 and 4 hours from the start of the simulation (Fig. 9). The cloud stops spread-
 378 ing and remains in the relatively thick anvil stage for longer compared with the control
 379 simulation.

380 At hour 4-5 of the simulation a diabatic heating "sandwich" pattern forms (Fig.
 381 5e), including:

- 382 • LW radiative cooling of about 10 K day^{-1} at the cloud top (Fig. 7g);
- 383 • LW radiative heating at the cloud base, with a smaller contribution from the SW
 384 radiative component just below the cloud top. The heating peaks at values be-
 385 tween 10 and 15 K day^{-1} (Fig. 7g);
- 386 • Latent heating by deposition contributes to most of the heating ($2\text{-}20 \text{ K day}^{-1}$)
 387 between 8 and 12 km altitude in the core of the cloud (Fig. 7f and 6e,h);
- 388 • Latent cooling by sublimation dominates the base of the cloud, reaching values
 389 of more than -50 K day^{-1} (Fig. 7f).

390 A reflection of the heating "sandwich" is seen in vertical velocity: a downdraft of
 391 up to 0.5 m s^{-1} at the cloud base, updrafts in the center and at the edges of the cloud
 392 of 0.05 to 0.2 m s^{-1} and a downwelling motion near cloud top (Fig. 5h). There are no
 393 clear boundaries between the updrafts and downdrafts, as two mixed layers form: one
 394 just below the cloud top and one in the central part of the cloud. Interestingly, depo-
 395 sition and sublimation often occur in what looks like the same location due to azimuthal
 396 and time averaging (Fig. 6e,g). The co-occurrence of deposition in sublimation is fur-
 397 ther supported by the highly turbulent cloud interior with several small convective cells,
 398 which gives rise to an uneven cloud top and cloud base, reminiscent of mammatus clouds
 399 (Garrett et al., 2010; Ferlay et al., 2014).

400 A strong upper level circulation pattern forms, driven mainly by ACRE and the
 401 associated turbulence (Figs. 5k, 8f-j), similar to the isolated cloud case. Latent heating
 402 is responsible for a weaker circulation close to the cloud base, at elevations between 5
 403 and 10 km. The radiatively-driven inflow at the cloud top forms a thin tropopause cir-
 404 rus cloud above the anvil cloud (Fig. 5b,c).

405 The final stage of cloud thinning is characterized by a weakening circulation that
 406 spreads with the cloud edge (Fig. 5c,f,i,l). The thin anvil cloud only slowly sediments
 407 due to the effects of radiative heating, which favor updraft motion. The radiative heat-
 408 ing is strongest near the spreading front, and weaker in the middle of the cloud, which
 409 sinks to lower levels, forming a bowl shaped cloud top with the tropopause cloud above
 410 (Fig 5f,i). The magnitude of microphysical rates decrease, with sublimation becoming
 411 dominant over the deposition and freezing (Fig. 6e-h). The clear-sky radiation drives
 412 part of the circulation only at the domain edges, where there is no stronger source of di-
 413 abatic heating (Figs 7d,h and 8d,i).

414 4.4 RCE

415 Finally, we analyze the contribution of several processes to the diabatic heating and
 416 circulation in a 80-day long simulation in radiative-convective equilibrium with no daily
 417 cycle of insolation. We analyze 48 timesteps (one every 2 hours) of output data from days
 418 70-74 of the simulation. We bin all gridpoints by their respective IWP in 50 bins, rather
 419 than attempt to detect and evaluate numerous convective lifecycles. The total diabatic
 420 heating reveals a familiar "sandwich" pattern with a strong in-cloud warming in the most
 421 ice-filled bins with cooling anomalies above (radiative cloud top cooling) and below it
 422 (sublimation), and a slightly negative background heating rate due to the LW emission
 423 by water vapor (Fig. 10d). We apply the method from C. S. Bretherton and Blossey (2005)
 424 to derive the mass streamfunction by integrating the vertical velocities in IWP binned
 425 columns. These results sample numerous convective systems with different properties and
 426 cloud top/base levels. Therefore we do not expect as sharp and strong circulation pat-
 427 terns as in our idealized simulations. Nevertheless, the reconstruction gives a circulation
 428 pattern with an inflow at levels below 10 km, outflow at 11-13 km, and an inflow just
 429 above the cloud top at 13-14 km (Fig. 10f), which is consistent with the idealized ex-
 430 periments. The streamfunction decomposition reveals important contributions to the cir-
 431 culation from both cloudy and clear-sky radiative effects, with a minor latent heating
 432 component (Fig. 10g-j). Unlike in the idealized experiments, the clear-sky component
 433 drives a large fraction of the circulation (Fig. 10i). The IWP binning gives equilibrium/climatological
 434 values; a high IWP is therefore well correlated with high moisture content, explaining
 435 the large clear-sky component of the streamfunction. The clear-sky cooling does not play
 436 a large role in idealized experiments, as the water vapor does not have enough time to
 437 fully adapt to the convective perturbation. The conclusions do not change in simulations
 438 that include the diurnal cycle of insolation (not shown).

4.5 Model resolution dependence

The horizontal grid spacing of 1 km only resolves part of the turbulent motions by the strong radiative and latent heating; the rest is generated by the subgrid turbulence scheme. To test the sensitivity of the results to the horizontal resolution we perform simulations of varying resolutions in the RCE setup. Increased model resolution increases the ratio of thin vs. all cirrus clouds, leading to a more positive net CRE (Fig. 11a). The main mechanisms leading to this resolution dependence are likely the turbulent motions, which are mainly parameterized at low resolutions and resolved at high resolutions. This is in contrast to Khairoutdinov et al. (2009), who found similar high cloud cover for horizontal resolutions of up to 1600 m compared with the 100 m benchmark simulation. However, they nudged the domain averaged thermodynamic fields and winds to the GATE Phase III field experiment observations (Fu et al., 1995) and used a simpler, one-moment microphysical scheme.

To better understand the effects of increased vertical and horizontal resolution on a single cloud lifecycle, we perform two additional simulations in the isolated convection setup:

- *VRES_con* in which we increase only the vertical resolution to 50 m between 8 and 15 km (while the layers between 5.5 and 8 km and 15 to 16.5 km have a resolution between 50 and 100 m);
- *HRES_con* in which we increase the horizontal resolution to 250 m and use the high vertical resolution from *VRES_con*.

The effects of increased vertical resolution to anvil properties and radiative effects are small (11b,c): the removal of IWC from the thicker part of the anvil is faster, which decreases the LW and SW CRE, accelerates the anvil evolution, and decreases its spreading. When additionally increasing the horizontal resolution, the cloud follows a similar evolution pattern in terms of averaged COD and its domain-averaged radiative effects (11b,c). The cloud covers a smaller area, which might be an artifact of a smaller horizontal model domain (160 km compared to 256 km). Interestingly, a closer look at the temporal evolution reveals significantly larger SW and LW CRE compared to *CTRL_con* and *VRES_con*. The finer horizontal resolution more than compensates for the faster IWC removal in the *VRES_con* simulation, leading to a thicker, (more net CRE negative) core of the cloud, and generating more clouds in the COD range of 0.3 to 3, which yield a larger LW CRE (Fig. S5). In summary, while increased horizontal and/or vertical resolution has an influence on the microphysical process rates and removal of ice from the atmosphere, it does not significantly change the evolution pathway nor the conclusions of our work.

4.6 Microphysical sensitivity tests

As the simulations of anvil cloud evolution were found to be very sensitive to details in the description of microphysics (Powell et al., 2012), we perform several microphysical sensitivity tests. In particular, we vary the upper limit of IC number concentration and implement a more realistic freezing scheme for temperatures below the homogeneous freezing temperature of water.

We perform simulations in which we change the upper IC number limit used in our simulations ($10 \cdot 10^6 \text{ kg}^{-1}$) to

- $0.5 \cdot 10^6 \text{ kg}^{-1}$ as used in the default P3 scheme;
- $100 \cdot 10^6 \text{ kg}^{-1}$.

The fraction of thin cirrus increases proportionally with the upper limit of ICs. Consequently, IClim0.5_rce decreases the net CRE by about 3 W m^{-2} , compared to the CTRL_rce simulation, while the IClim100_rce has just the opposite effect (Fig. 11a). Interestingly

488 the impact on the single convective cloud and its lifecycle is different: decreasing the limit
 489 does not allow the initial formation of a very thick anvil cloud, and leads to a thinner
 490 and smaller cloud, with a more positive net CRE. On the other hand, IClim100_conv al-
 491 lows a formation of a thicker and longer-lived cloud, which, however, does not change
 492 its integrated CRE much over the course of the convective lifecycle (Fig. 11b,c).

493 Moreover, P3 does not have a proper description of freezing below the homogeneous
 494 freezing temperature of water (-38°C). The deposition freezing parameterization by Cooper
 495 (1986), valid in the mixed-phase temperature range, is used also at temperatures colder
 496 than -38°C , leading to an overestimation of freezing events. The high number of newly
 497 nucleated ICs at cirrus levels is therefore limited by the upper IC number limit. We try
 498 to avoid the frequent use of the unphysical IC limit by parameterizing the freezing at
 499 temperatures colder than -38°C using the homogeneous freezing scheme from X. Liu and
 500 Penner (2005), and a heterogeneous freezing based on the laboratory results from Möhler
 501 et al. (2006). The heterogeneous freezing scheme assumes a dust concentration of 2 ice
 502 nucleating particles per liter. This number is based on the simulated dust concentrations
 503 in TWP by ECHAM-HAM climate model (Gasparini & Lohmann, 2016). Interestingly,
 504 the implementation of the new freezing scheme (*NFRZ_rce*) does not change the net CRE,
 505 despite forming about 5% less thin cirrus compared to *CTRL_rce* (Fig 11a). *NFRZ_conv*
 506 decreases the lifetime of the detrained anvil cloud due to a decrease in the frequency of
 507 ice nucleation events, but does not change the net CRE integrated over the whole anvil
 508 lifecycle (Fig. 11b,c). Such behavior may also explain why the net CRE balance does
 509 not change between the control and *NFRZ_rce* simulations.

510 4.7 Modelling results in the context of the observed cloud radiative prop- 511 erties

512 Figure 12 shows the observed probability density function of the outgoing LW ra-
 513 diation (OLR) - albedo pairings for the TWP during July and August as described in
 514 Hartmann and Berry (2017). The green contours represent the analogous PDF computed
 515 from the 80-day long RCE simulation, averaged to 32×32 km to correspond with the ob-
 516 served CERES pixel dimensions. They follow the peak of the observed distribution but
 517 show less variability in both albedo and OLR. The smaller number of sample points re-
 518 sulting from horizontal averaging, together with the absence of large-scale dynamical vari-
 519 ability are responsible for its smaller spread compared with observations. Moreover, the
 520 mode of the distribution is shifted towards larger albedo and smaller OLR values, indica-
 521 tive of an overestimation of thin cirrus. On the other hand, the isolated cloud simula-
 522 tion follows the peak of the observed PDF but starts at a higher OLR indicative of a too
 523 low cloud top compared to the observed deep convective clouds. The isolated convec-
 524 tion simulation differs from the isolated cloud simulation in that it starts at clear-sky
 525 conditions, quickly grows to a high albedo and low OLR deep convective core, which grad-
 526 ually thins by following the peak of the observed PDF. After about 14 hours, the first
 527 convective lifecycle reaches the final thin cirrus stage, with the radiative properties very
 528 close to the initial clear-sky conditions. Moreover, the duration of the convective life-
 529 cycle qualitatively agrees with the results from Wall and Hartmann (2018), which were able
 530 to track the tropical convective systems with geostationary satellite data for about 10
 531 hours after the peak of convective activity. Fig. 12 shows that our idealized modelling
 532 setup can reproduce average aspects of the tropical cloud radiative properties and its evo-
 533 lution, supporting our main findings of the importance of diabatic processes on the anvil
 534 cloud evolution.

5 Discussion

5.1 Drivers of anvil evolution

Our results largely agree with previous literature on the importance of ACRE for the maintenance and radiative effects of the anvil lifecycle. Simulations without the effects of ACRE could not achieve a near-cancellation of the SW and LW CRE as observed in the deep tropics, leading instead to a strongly negative net CRE. Radiative heating promotes the formation and maintenance of thin anvils, which is similar to the results by Hartmann et al. (2018) who used a very simple cloud geometry. We find the horizontal spreading of the cloud to be the key feature influencing the radiative effects integrated over the whole convective lifecycle. We attributed a large share of the spreading to the in-atmospheric cloud radiative heating, as the cloud did not spread in the *NO ACRE* simulation.

The isolated cloud case closely follows the thick cirrus simulation from Schmidt and Garrett (2013). While they studied only the first hour of a high resolution limited-area model output, we used a coarser resolution and a larger domain size to be able to monitor later stages of cloud evolution. Similarly to their study, we find the early stage of evolution in the isolated cloud setup to be dominated by radiatively driven turbulence at the cloud top and cloud base and the spreading mixed layer (Fig. 13a). After a few minutes of simulations, however, the contribution from latent heating and cooling become dominant in the lower half of the cloud, while the upper third of the cloud is dominated by the radiatively driven circulations throughout the lifecycle. The contribution of latent heating gradually decreases with the thinning of the cloud, when the turbulence is replaced by weaker motions, mainly radiatively driven.

The isolated cloud simulations qualitatively agree with the Lilly (1988) model of the deep convective outflow as an intrusion of nearly equally buoyant air with isotropic turbulence into stably stratified environmental air. The initial convective outflow can be thought of as a large spherical air parcel. When the parcel hits the stable environment with potential temperature increasing with height, it has to flatten to form a pancake-like spreading pattern and generate predominantly horizontal and isentropic laminar flows (Fig. 3j-1).

The later stage of the isolated convective case evolution is, similarly to the isolated cloud case, dominated by a combination of radiative and turbulent driving at the cloud top, and latent heating at the cloud base, which gradually decreases in strength due to the thinning of the cloud and the smaller microphysical process rates (Fig. 13b). At hour 13 of the simulation, new convective activity starts, which again increases the significance of latent heating. Our study highlights the importance of the interaction of radiative and latent processes for the in-cloud convection and inhomogeneities, agreeing with results from Dobbie and Jonas (2001) that studied cirrus of COD between 1 and 2.

We have shown how an isolated deep convective system in the absence of large scale ascent evolves until it reaches the thin cirrus stage. At this stage, the cloud properties are similar to those observed in persistent tropical tropopause cirrus, which have been found to be in a delicate balance between microphysics, radiation, and the generated internal cloud dynamics (T. P. Dinh et al., 2010; T. Dinh et al., 2012). The evolution of both our idealized cloud and isolated convection suggest that the anvil cloud ends its lifecycle by a transition to a similar self-sustained thin cirrus stage.

5.2 Shortcomings of the modeling setup

The absence of ocean coupling and the relatively small domain prevents us from studying other proposed mechanisms behind the triggering and occurrence of tropical deep convection and its CRE budget. Ramanathan and Collins (1991) and Hartmann, Moy, and Fu (2001) proposed a mechanism that couples tropical convection, the associated cloud albedo, sea surface temperatures, and atmospheric circulations by a self-regulating feedback process.

587 Wall et al. (2018)’s observational study also supports the idea of a tight coupling
 588 between the triggering of deep convection and the sea surface temperatures in the TWP.
 589 Our idealized study rather focuses on the drivers of the evolution of convection and the
 590 detrained anvil clouds, once the conditions are right for its triggering. Our primary fo-
 591 cus is on the sub-daily scale, which is too short to be significantly affecting sea surface
 592 temperatures. Sea surface temperature mediated feedbacks have been found to influence
 593 simulations in an RCE setup (Coppin & Bony, 2017) and will therefore be included in
 594 our future work.

595 Convective strength, anvil cloud extent, and their properties are also modulated
 596 by the daily cycle of insolation (Chen & Houze, 1997; Dai, 2001). Ruppert and Klocke
 597 (2019) show that the diurnal peak in the cloud radiative heating increases the vertical
 598 velocities within anvils and leads to an anvil cloud peak in the afternoon. Similarly, the
 599 anvil lifecycle was found to be suppressed during nighttime. Including the daily cycle
 600 of insolation would therefore modulate the cloud evolution and radiative effects. In ad-
 601 dition, the cloud evolution in our study is simulated in the absence of a large-scale forc-
 602 ing and also cannot feed back on larger scale circulations. Therefore the gravity waves
 603 generated by the initial burst of convection can return back towards the middle of the
 604 domain via the periodic horizontal boundary conditions. Figure 12 show, however, that
 605 the listed shortcomings do not prevent us from simulating clouds that fit within the range
 606 of the observations from the TWP.

607 6 Conclusions

608 The net CRE in the tropics range from very negative, SW dominated deep con-
 609 vective cores, to near neutral or moderately positive for intermediately thick anvil clouds,
 610 to positive for thin anvils and other high clouds that are not directly related to detrained
 611 ice from convection. The convective lifecycle starts with a convective instability and up-
 612 draft motion. Updrafts are associated with a large latent heat release due to cloud droplet
 613 condensation and freezing, and depositional growth of newly nucleated ice crystals. La-
 614 tent heat release is the dominant factor in the deep circulation pattern that develops in
 615 the early convective stage, with the low level inflow, upper level outflow, and the slow
 616 subsidence far from the convective core. This circulation is also responsible for the large
 617 initial spreading of the cloud, reaching horizontal velocities beyond 5 m s^{-1} . About 3
 618 hours after the convective initiation, the cloud has spread horizontally more than 50 km
 619 from the convective core, developing a thick stratiform anvil with a strong sandwich-like
 620 heating pattern, which can be summarized by:

- 621 • A LW cooling at the cloud top;
- 622 • A LW warming at and near the cloud base and cloud edge;
- 623 • Additional warming in the cloud interior by latent heating due to the depositional
 624 growth of ice crystals;
- 625 • A strong cooling at and just below the cloud base due to ice crystal sublimation.

626 The differential heating and cooling are found to drive within-anvil turbulent motions
 627 at horizontal scales smaller than 5-10 km. However, the mixed layer does not spread through
 628 the whole cloud: in fact, we observe a strong small-scale overturning below the cloud top,
 629 and a weaker one close to the cloud base. While the radiative and latent contributions
 630 are closely related, we find the upper third of the cloud to be predominantly driven by
 631 in-atmospheric cloud radiative effects. In contrast, latent heating drives the evolution
 632 and circulations in the lower part of the cloud. Within-anvil convection and turbulence
 633 slowly decrease in strength with the thinning and spreading of the cloud, until the lam-
 634 inar motions become dominant at cloud optical depths between about 5 and 10. Inter-
 635 estingly, the radiatively driven circulation at the cloud top is responsible for the forma-
 636 tion of thin tropopause cirrus. The results of the idealized isolated cloud and isolated

Table 1. Simulation terminology and their respective properties

Simulation	Description
1. Isolated cloud	
<i>CTRL_cld</i>	256x256 horizontal gridboxes with 1 km resolution; 128 vertical levels with 250 m resolution in the upper troposphere
<i>NO ACRE</i>	As <i>CTRL_cld</i> but no interactive ACRE
<i>NO SUBI</i>	As <i>CTRL_cld</i> but with no sublimation of ICs
<i>NO DEPO</i>	As <i>CTRL_cld</i> but no deposition of vapor on ICs
<i>NO NUCI</i>	As <i>CTRL_cld</i> but with no new nucleation of ICs
<i>NO SEDI</i>	As <i>CTRL_cld</i> but with no sedimentation ICs
2. Isolated conv.	
<i>CTRL_con</i>	256x256 horizontal gridboxes with 1 km resolution; 128 vertical levels with 250 m resolution in the upper troposphere
<i>VRES_con</i>	As <i>CTRL_con</i> but with 256 vertical levels with 50 m upper tropospheric grid spacing
<i>HRES_con</i>	As <i>VRES_con</i> but with 640x640 horizontal boxes of 250 m grid spacing
<i>NFRZ_con</i>	As <i>CTRL_con</i> but with different freezing for temperatures colder than -38°C
3. RCE	
<i>CTRL_rce</i>	128x128 horizontal gridboxes with 1 km resolution; 128 vertical levels with 250 m resolution in the upper troposphere
<i>CTRL0.25-7_rce</i>	As <i>CTRL_rce</i> but with a horizontal grid spacing of 0.25, 0.5, 2, 3, 5, and 7 km
<i>IClim0.5_rce</i>	As <i>CTRL_rce</i> but with the upper IC number limit of $0.5 \cdot 10^3 \text{ kg}^{-1}$
<i>IClim100_rce</i>	As <i>CTRL_rce</i> but with the upper IC number limit of $100 \cdot 10^3 \text{ kg}^{-1}$
<i>NFRZ_rce</i>	As <i>CTRL_rce</i> but with different freezing for temperatures colder than -38°C

637 convective simulations qualitatively agree with averages from the radiatively convective
638 equilibrium simulation, with the exception of the clear-sky effects which are very impor-
639 tant in RCE (Hartmann & Larson, 2002).

640 Our findings confirm that small-scale processes are important for the anvil cloud
641 lifecycle. Such microphysical, radiative, and dynamical processes significantly impact the
642 cloud development and hence cloud radiative effects and climate. Current general cir-
643 culation models, that are used for future climate and cloud feedback estimates, have up-
644 per tropospheric vertical and horizontal resolutions orders of magnitude larger than the
645 scales discussed in this work and often have difficulties in simulating anvil clouds (Wall
646 & Hartmann, 2018). Results from studies on high cloud responses to increased green-
647 house gas concentrations (Hartmann & Larson, 2002; Mauritsen & Stevens, 2015; Bony
648 et al., 2016) using crude descriptions of the small-scale processes should therefore be re-
649 visited. The new generation of global climate models, even those able to directly sim-
650 ulate deep convection, might still not simulate the small-scale processes driving the anvil
651 evolution in a reliable way. Our idealized modelling setup could therefore provide a bench-
652 mark for parameterizations in models both with parametrized as well as directly resolved
653 deep convection.

654 Acknowledgments

655 We acknowledge support from the Swiss National Science Foundation grant P2EZP2-
656 178485 (B.G.), National Science Foundation through grant ATG-1549579 (B.G. and P.B.),
657 Department of Energy (DOE) Office of Science Early Career Award Program (J.F.). The
658 work of coupling P3 with SAM was carried out by G.L. and J.F. who were supported

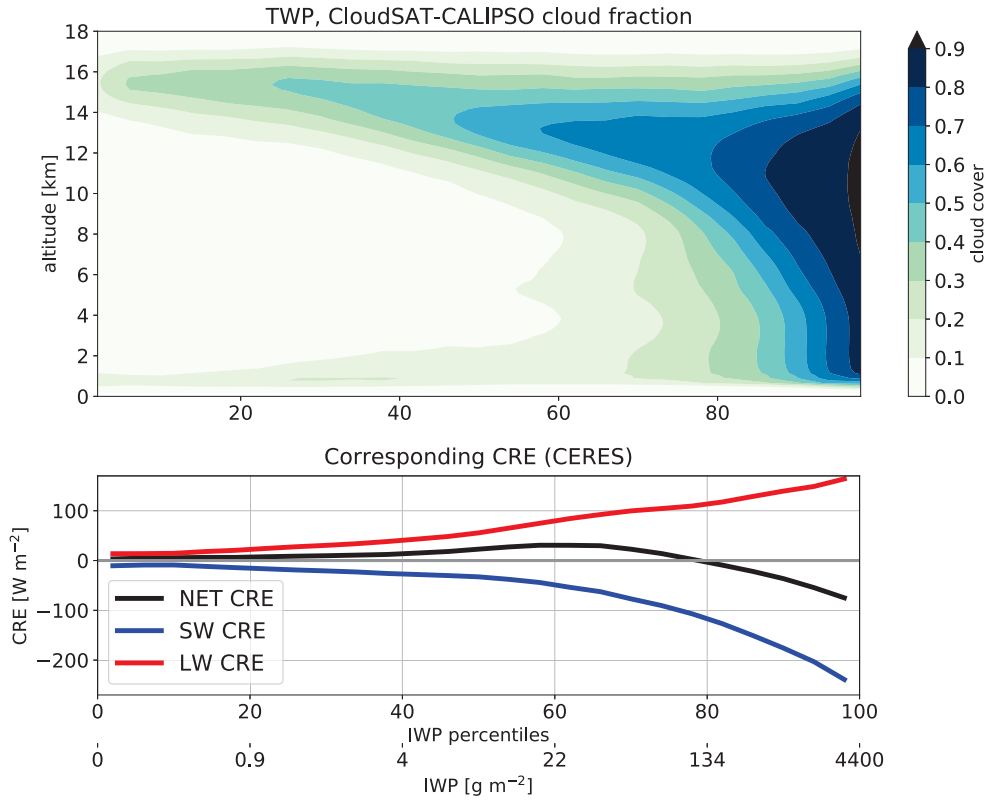


Figure 1. CCCM-derived cloud fraction binned into 25 IWP percentiles for the TWP. Below are plotted the corresponding CRE.

659 by the Climate Model Development and Validation program of the DOE Climate and
 660 Environmental Sciences Division. Supporting data will be made available on a public
 661 repository when the paper is published. We acknowledge Phil Rasch and Marina Dütsch
 662 for insightful discussions that improved this study.

663 References

- 664 Ackerman, T. P., Liou, K.-N., Valero, P. J. F., & Pfister, L. (1988). Heating Rates
 665 in Tropical Anvils. *Journal of Atmospheric Sciences*, *45*(10), 1606–1623.
- 666 Berry, E., & Mace, G. G. (2014). Cloud properties and radiative effects of the Asian
 667 summer monsoon derived from A-Train data. *Journal of Geophysical Research*
 668 *Atmospheres*, *119*, 9492–9508. doi: 10.1002/2014JD021458
- 669 Bony, S., Stevens, B., Coppin, D., Becker, T., Reed, K. A., Voigt, A., & Medeiros,
 670 B. (2016). Thermodynamic control of anvil cloud amount. *Proceed-*
 671 *ings of the National Academy of Sciences*, *113*(32), 8927–8932. Retrieved
 672 from <http://www.pnas.org/content/113/32/8927.abstract> doi:
 673 10.1073/pnas.1601472113
- 674 Bretherton, C. (1988). Group Velocity and the Linear Response of Stratified Fluids
 675 to Internal Heat or Mass Sources. *Journal of the Atmospheric Sciences*, *45*(1),
 676 81–94. doi: 10.1175/1520-0469(1988)045<0081:gvatlr>2.0.co;2
- 677 Bretherton, C. S., & Blossey, P. N. (2005). An Energy-Balance Analysis of Deep
 678 Convective Self-Aggregation above Uniform SST. *Journal of Atmospheric Sci-*

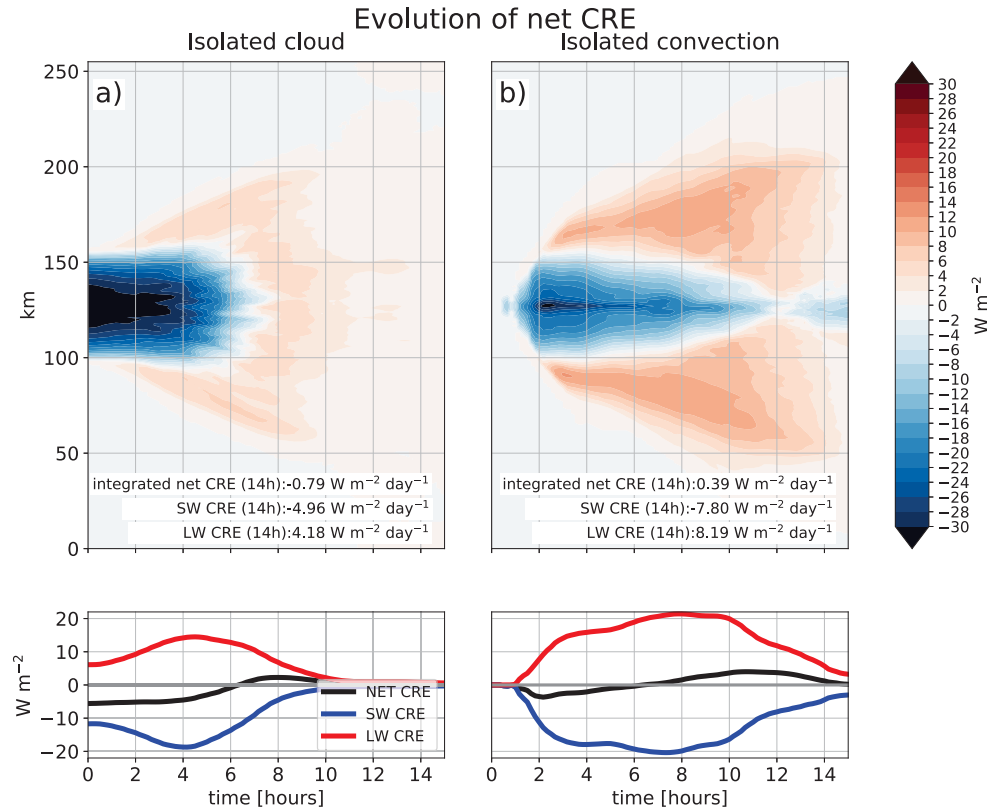


Figure 2. CRE evolution for simulations of an isolated cloud (a) and isolated convection (b). The contour plots are computed by averaging over one of the horizontal dimensions. The lower plot represents the domain averaged CRE. The numbers represent CRE values integrated over the whole lifecycle.

- 679 *ences*. doi: 10.1007/978-3-540-48605-3{_}23
- 680 Charney, J. G. (1963). A Note on Large-Scale Motions of the Tropics. *Journal of the*
- 681 *Atmospheric Sciences*, 20, 607–609.
- 682 Chen, S. S., & Houze, R. A. J. (1997). Diurnal variation and life-cycle of deep convec-
- 683 tive systems over the tropical Pacific warm pool. *Quarterly Journal of the*
- 684 *Royal Meteorological Society*, 123(538), 357–388.
- 685 Cooper, W. A. (1986). Ice Initiation in Natural Clouds. *Meteorological Monographs*,
- 686 43, 29–32. Retrieved from <https://doi.org/10.1175/0065-9401-21.43.29>
- 687 doi: 10.1175/0065-9401-21.43.29
- 688 Coppin, D., & Bony, S. (2017). Internal variability in a coupled general circula-
- 689 tion model in radiative-convective equilibrium. *Geophysical Research Letters*,
- 690 44(10), 5142–5149. doi: 10.1002/2017GL073658
- 691 Dai, A. (2001). Global precipitation and thunderstorm frequencies. Part II: Di-
- 692 urnal variations. *Journal of Climate*, 14(6), 1112–1128. doi: 10.1175/1520-
- 693 -0442(2001)014(1112:GPATFP)2.0.CO;2
- 694 Dinh, T., Durran, D. R., & Ackerman, T. (2012). Cirrus and water vapor transport
- 695 in the tropical tropopause layer Part 1: A specific case modeling study. *Atmo-*
- 696 *spheric Chemistry and Physics*, 12(20), 9799–9815. doi: 10.5194/acp-12-9799-
- 697 -2012

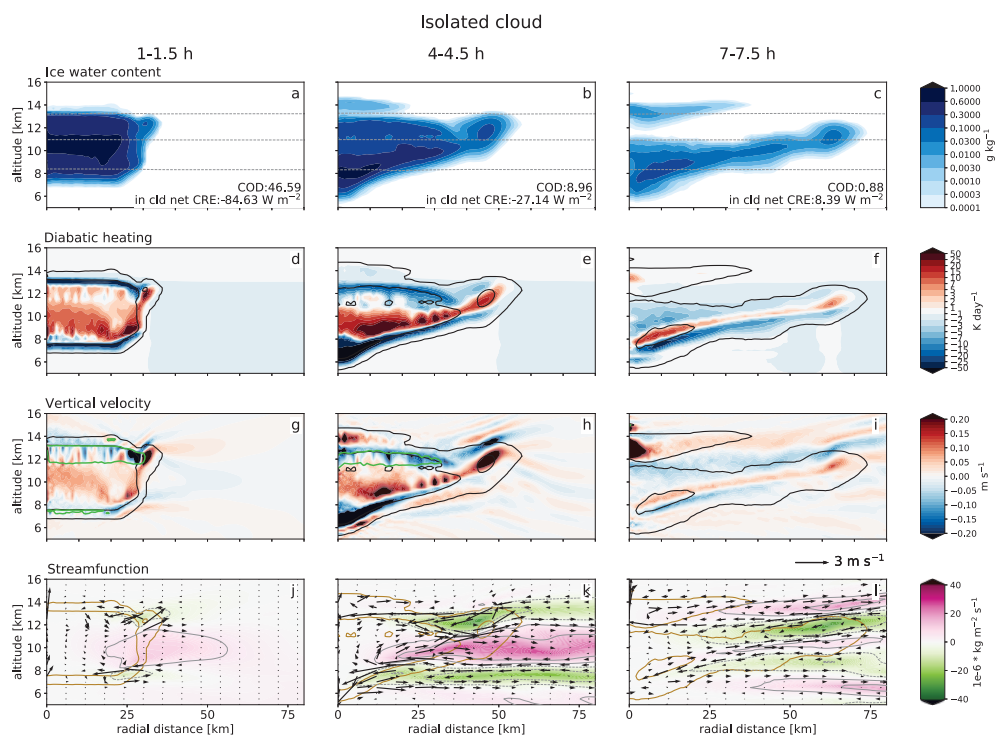


Figure 3. Evolution of the isolated high cloud: IWC (a-c), diabatic heating (d-f), vertical velocity (g-i), and streamfunction and wind fields (j-l). The plotted timesteps are representative of the initial, mature, and late stage of cloud evolution. The panels a-c include temperature iso-lines and in-cloud COD and CRE values. The green contours in panels g-i highlight areas of high spatial variability of vertical velocity. The plotted quantities are azimuthally averaged with respect to the center of the domain. The dashed lines in a-c are isotherms of -20 , -40 and -60°C . Black or brown contour lines represent IWC contours of 0.1 and 0.0001 g kg^{-1} . The vertical velocity vectors are multiplied by a factor of 4 to give a better visual representation of circulations.

- 698 Dinh, T. P., Durran, D. R., & Ackerman, T. P. (2010). Maintenance of tropical
 699 tropopause layer cirrus. *Journal of Geophysical Research Atmospheres*,
 700 *115*(D2), 1–15. doi: 10.1029/2009JD012735
- 701 Dobbie, S., & Jonas, P. (2001). Radiative influences on the structure and lifetime
 702 of cirrus clouds. *Quarterly Journal of the Royal Meteorological Society*(127),
 703 2663–2682.
- 704 Durran, D. R., Dinh, T., Ammerman, M., & Ackerman, T. (2009). The Mesoscale
 705 Dynamics of Thin Tropical Tropopause Cirrus. *Journal of the Atmospheric
 706 Sciences*, *66*(9), 2859–2873. doi: 10.1175/2009jas3046.1
- 707 Fan, J., Comstock, J. M., & Ovchinnikov, M. (2010). The cloud condensation nuclei
 708 and ice nuclei effects on tropical anvil characteristics and water vapor of
 709 the tropical tropopause layer. *Environmental Research Letters*, *5*(4). doi:
 710 10.1088/1748-9326/5/4/044005
- 711 Fan, J., Leung, L. R., Rosenfeld, D., Chen, Q., Li, Z., Zhang, J., & Yan, H. (2013).
 712 Microphysical effects determine macrophysical response for aerosol impacts
 713 on deep convective clouds. *Proceedings of the National Academy of Sciences*,
 714 *110*(48), E4581–E4590. doi: 10.1073/pnas.1316830110
- 715 Ferlay, N., Garrett, T. J., & Minvielle, F. (2014). Satellite Observations of an Un-

Isolated cloud - sensitivity tests at 7-7.5 h: ice water content

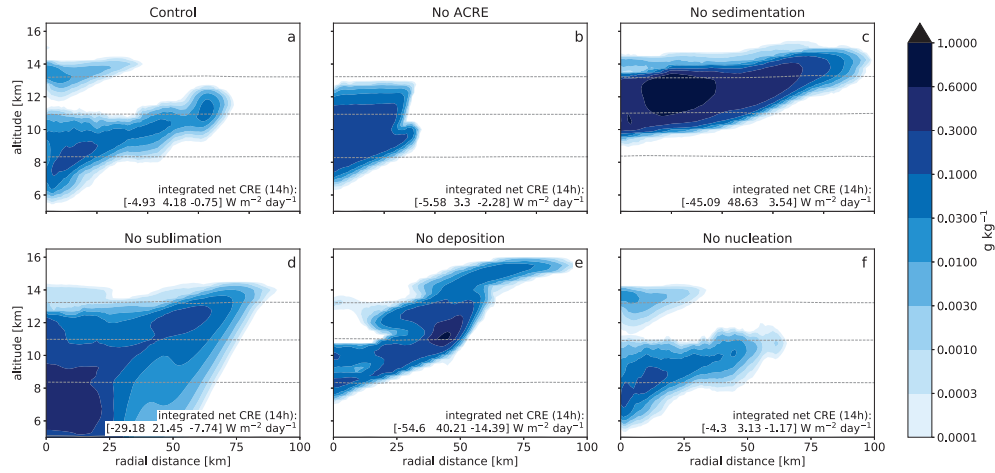


Figure 4. Sensitivity simulations for the isolated clouds. The numbers at the bottom of the panels represent the integrated values of SW, LW, and net CRE over the first 14 hours of the respective simulations.

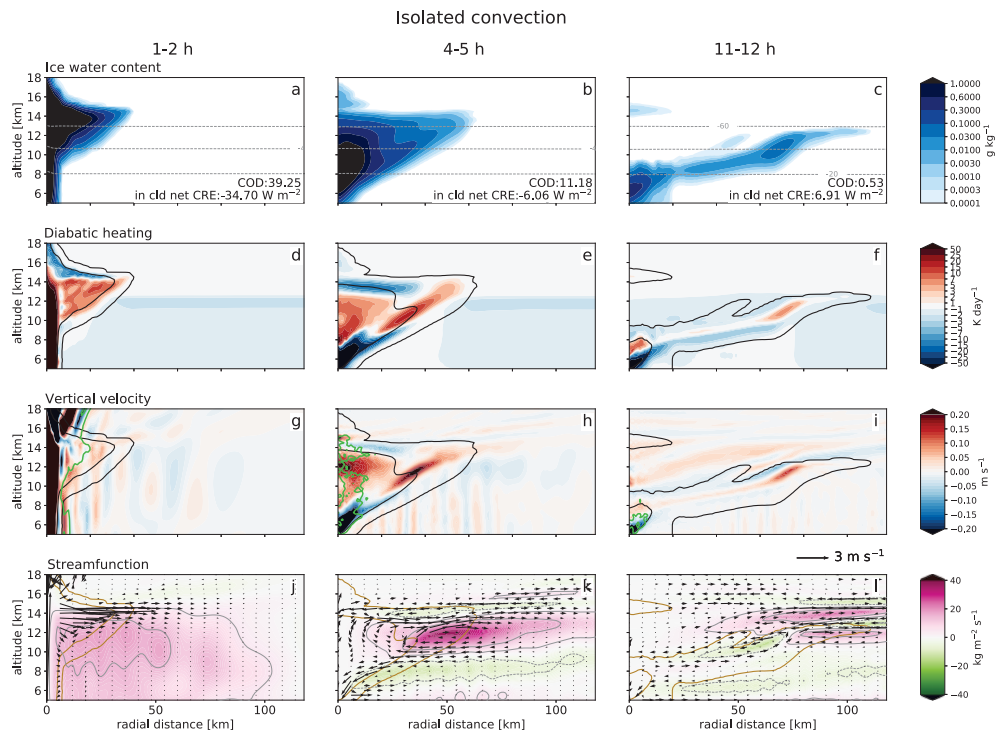


Figure 5. As in Figure 3, but for the isolated convection.

716
717
718

usual Cloud Formation near the Tropopause. *Journal of the Atmospheric Sciences*, 71(10), 3801–3815. doi: 10.1175/jas-d-13-0361.1
Fu, Q., Krueger, S. K., & Liou, K. N. (1995). Interactions of Radiation and Con-

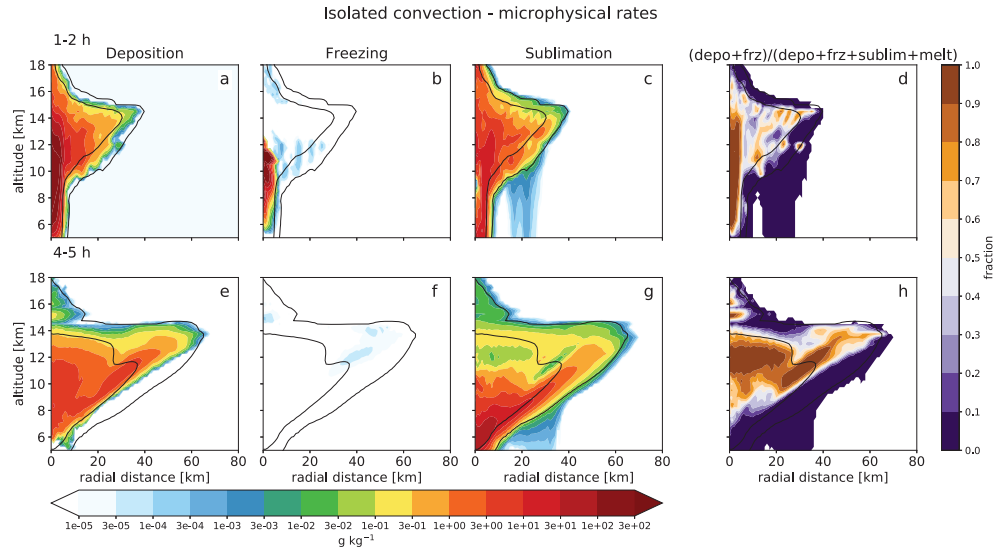


Figure 6. Evolution of the selected microphysical process rates for the isolated convective case. The last column represents the ratio between the absolute values of sources and sinks. The black contour lines represent IWC contours of 0.1 and 0.0001 g kg^{-1} .

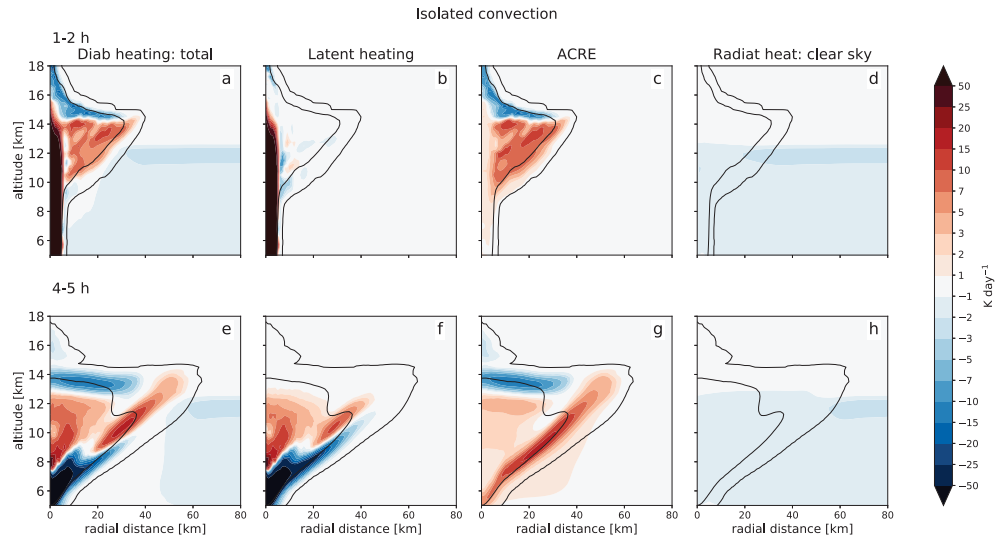


Figure 7. Decomposition of the diabatic heating sources for isolated convection. Black contour lines represent IWC contours of 0.1 and 0.0001 g kg^{-1} .

719 vection in Simulated Tropical Cloud Clusters. *Journal of the Atmospheric Sci-*
 720 *ences*, 52(9), 1310–1328. doi: 10.1175/1520-0469(1995)052<1310:ioraci>2.0.co;
 721 2
 722 Garrett, T. J., Navarro, B. C., Twohy, C. H., Jensen, E. J., Baumgardner, D. G.,
 723 Bui, P. T., ... Weinstock, E. M. (2005). Evolution of a Florida Cir-
 724 rus Anvil. *Journal of the Atmospheric Sciences*, 62(7), 2352–2372. doi:
 725 10.1175/JAS3495.1

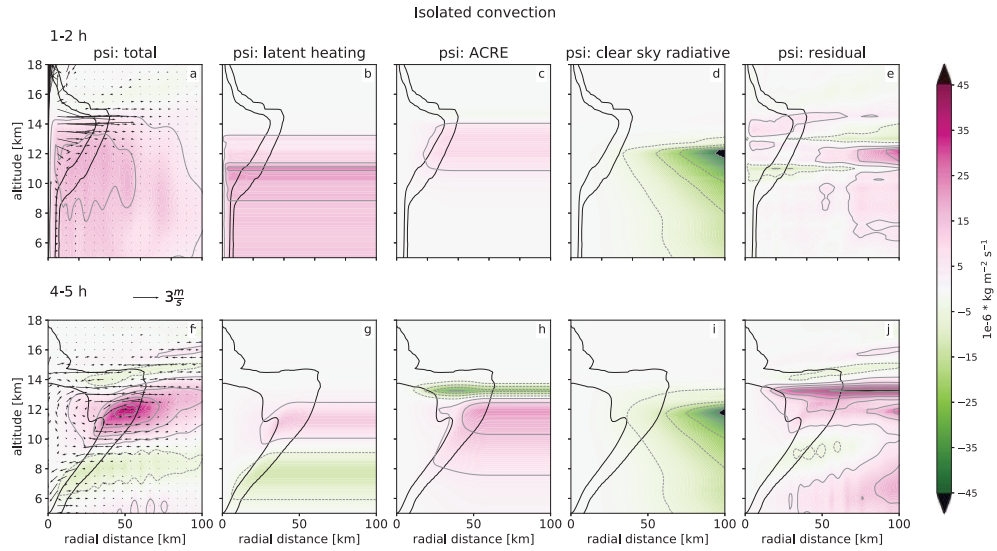


Figure 8. Decomposition of the streamfunction for isolated convection. Black contour lines represent IWC contours of 0.1 and 0.0001 g kg^{-1} . The panels a and f show also wind vectors. Vertical winds are multiplied by a factor of 4.

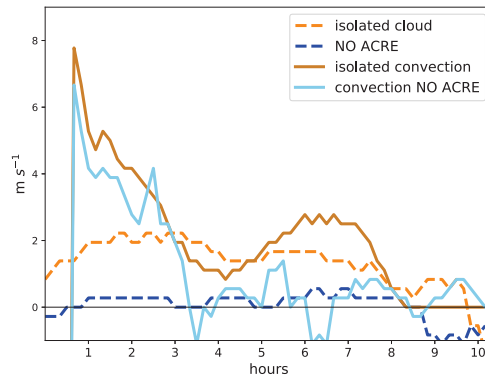


Figure 9. Spreading velocity of the cloud for isolated cloud and isolated convective simulations. The velocity is calculated from the azimuthally averaged IWP spreading front defined by the outermost gridpoint that reaches IWP value of 0.005 g m^{-2} .

- 726 Garrett, T. J., Schmidt, C. T., Kihlgren, S., & Cornet, C. (2010). Mammatus
 727 Clouds as a Response to Cloud-Base Radiative Heating. *Journal of the Atmo-*
 728 *spheric Sciences*, 67(12), 3891–3903. doi: 10.1175/2010JAS3513.1
 729 Gasparini, B., & Lohmann, U. (2016). Why cirrus cloud seeding cannot substantially
 730 cool the planet. *Journal of Geophysical Research: Atmospheres*, 121. doi: 10
 731 .1002/2015JD024666
 732 Gasparini, B., Meyer, A., Neubauer, D., Münch, S., & Lohmann, U. (2018). Cirrus
 733 cloud properties as seen by the CALIPSO satellite and ECHAM-HAM global
 734 climate model. *Journal of Climate*, 31(5). doi: 10.1175/JCLI-D-16-0608.1
 735 Gehlot, S., & Quaas, J. (2012). Convection-climate feedbacks in the ECHAM5
 736 general circulation model: Evaluation of cirrus cloud life cycles with ISCCP

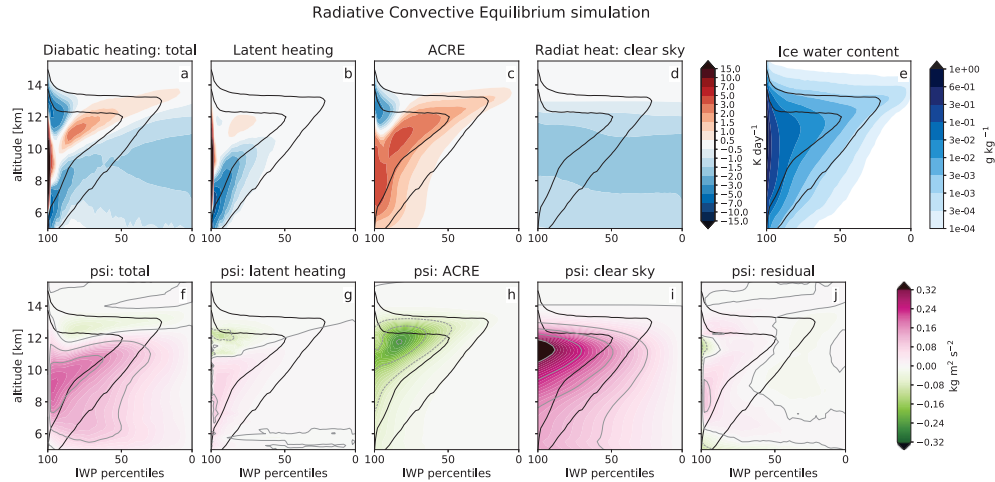


Figure 10. Decomposition of diabatic heating and streamfunction into its components for the RCE simulation. Black contour lines represent cloud fractions of 0.1 and 0.5.

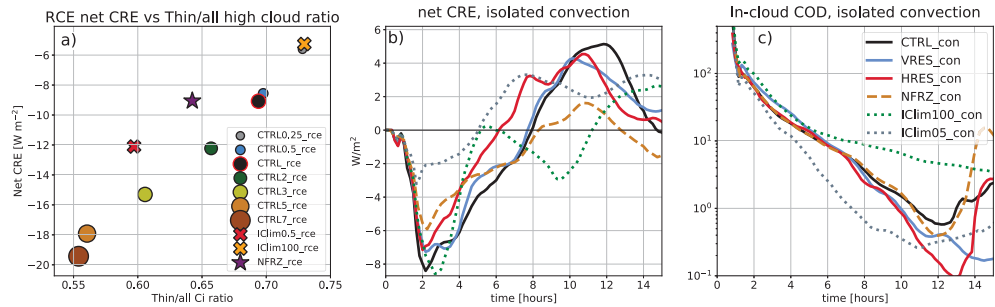


Figure 11. Sensitivity simulations for RCE (a) and isolated convection (b,c) setups. (a) The ratio of thin vs. all cirrus where thin cirrus are all high clouds that have a net positive CRE, i.e. with COD larger than 4. (b,c) Time evolution of domain averaged net CRE and in-cloud COD for the isolated convective simulations. In b) only the middle 160 km of the domain are considered, to account for the smaller horizontal grid dimension in *HRES.con*.

737 satellite data from a lagrangian trajectory perspective. *Journal of Climate*,
 738 *25*(15), 5241–5259. doi: 10.1175/JCLI-D-11-00345.1
 739 Harrop, B. E., & Hartmann, D. L. (2016). The role of cloud radiative heating
 740 within the atmosphere on the high cloud amount and top-of-atmosphere cloud
 741 radiative effect. *Journal of Advances in Modeling Earth Systems*, *8*. doi:
 742 10.1002/2013MS000282.Received
 743 Hartmann, D. L., & Berry, S. E. (2017). The Balanced Radiative Effect of Tropical
 744 Anvil Clouds. *Journal of Geophysical Research : Atmospheres*, *122*. doi: 10
 745 .1002/2017JD026460
 746 Hartmann, D. L., Gasparini, B., Berry, S. E., & Blossey, P. N. (2018). The Life Cy-
 747 cle and Net Radiative Effect of Tropical Anvil Clouds. *Journal of Advances in*
 748 *Modeling Earth Systems*, *10*(12), 3012–3029. doi: 10.1029/2018MS001484
 749 Hartmann, D. L., Holton, J. R., & Fu, Q. (2001). The heat balance of the tropical
 750 tropopause, cirrus, and stratospheric dehydration. *Geophys. Res. Lett.*, *28*(10),
 751 1969–1972.

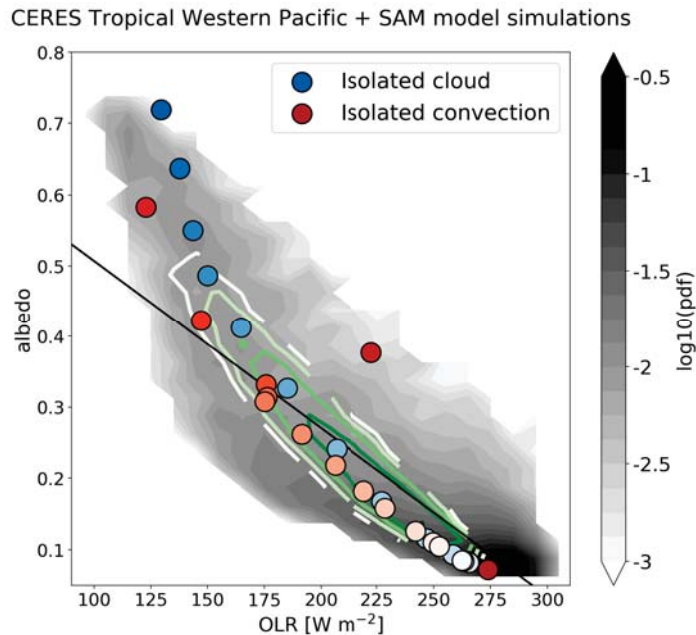


Figure 12. Probability density of OLR and albedo from CERES pixel measurements from the TWP (12°S to 12°N, 150°E to 170°E). The green contour lines show the same distribution derived from the RCE simulation. Blue circles represent the average over the cloudy part of the domain for the isolated cloud case, while the red circles represent the same for the isolated convective case. The circles are spaced by 1 simulation hour; the color of the circles is fading together with the time evolution of the cloud. The black line indicates the approximate location of the net CRE neutral line. Points above (below) the line have a negative (positive) net CRE.

- 752 Hartmann, D. L., & Larson, K. (2002). An important constraint on tropical cloud -
 753 climate feedback. *Geophysical Research Letters*, *29*(20), 1951:12. doi: 10.1029/
 754 2002GL015835
- 755 Hartmann, D. L., Moy, L. A., & Fu, Q. (2001). Tropical convection and the energy
 756 balance at the top of the atmosphere. *Journal of Climate*, *14*(24), 4495–4511.
 757 doi: 10.1175/1520-0442(2001)014<4495:TCATEB>2.0.CO;2
- 758 Heymsfield, A. J., Krämer, M., Luebke, A., Brown, P., Cziczo, D. J., Franklin, C.,
 759 ... Tricht, K. V. (2017). Cirrus Clouds. *Meteorological Monographs*, *58*, 1–2.
 760 Retrieved from [http://journals.ametsoc.org/doi/10.1175/AMSMONOGRAPHS](http://journals.ametsoc.org/doi/10.1175/AMSMONOGRAPHS-D-16-0010.1)
 761 [-D-16-0010.1](http://journals.ametsoc.org/doi/10.1175/AMSMONOGRAPHS-D-16-0010.1) doi: 10.1175/AMSMONOGRAPHS-D-16-0010.1
- 762 Heymsfield, A. J., Krämer, M., Wood, N. B., Gettelman, A., Field, P. R., & Liu,
 763 G. (2017). Dependence of the Ice Water Content and Snowfall Rate on
 764 Temperature, Globally: Comparison of in Situ Observations, Satellite Active
 765 Remote Sensing Retrievals, and Global Climate Model Simulations. *Jour-*
 766 *nal of Applied Meteorology and Climatology*, *56*(1), 189–215. Retrieved from
 767 <http://journals.ametsoc.org/doi/10.1175/JAMC-D-16-0230.1> doi:
 768 10.1175/JAMC-D-16-0230.1
- 769 Houze, R. A. J. (1982). Clusters and Large-Scale in the Tropics Vertical Motions.
 770 *Journal of the Meteorological Society of Japan*, *60*(1), 396–410.
- 771 Iacono, M. J., Delamere, J. S., Mlawer, E. J., Shephard, M. W., Clough, S. A., &
 772 Collins, W. D. (2008). Radiative forcing by long-lived greenhouse gases: Cal-
 773 culations with the AER radiative transfer models. *Journal of Geophysical*

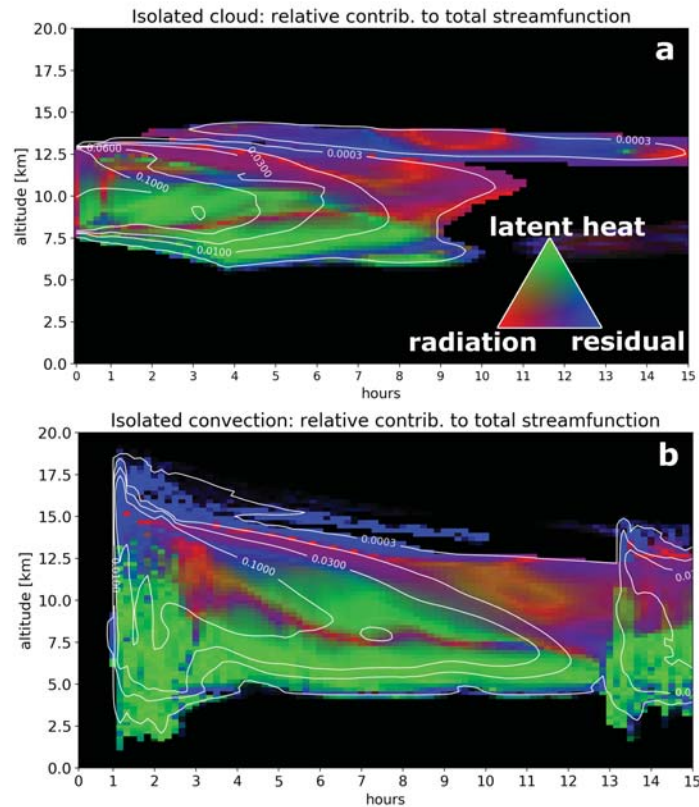


Figure 13. Relative importance of radiation (red), latent heating (green) and the residual (blue, mainly related to turbulent motions) to the total streamfunction for the isolated cloud (a) and isolated convection (b). White contours represent equal IWC lines. A mixture of colors represents a mixture of processes.

- 774 *Research Atmospheres*, 113(13), 2–9. doi: 10.1029/2008JD009944
- 775 Jackson, R. C., McFarquhar, G. M., Fridlind, A. M., & Atlas, R. (2015). The de-
 776 pendence of cirrus gamma size distributions expressed as volumes in N_0 - λ - μ
 777 phase space and bulk cloud properties on environmental conditions: Results
 778 from the Small Ice Particles in Cirrus Experiment (SPARTICUS). *Journal of*
 779 *Geophysical Research : Atmospheres*, 120, 10351–10377.
- 780 Jensen, E. J., Pfister, L., Bui, T.-P., Lawson, P., & Baumgardner, D. (2009). Ice
 781 nucleation and cloud microphysical properties in tropical tropopause layer cir-
 782 rus. *Atmospheric Chemistry and Physics Discussions*, 9, 20631–20675. doi:
 783 10.5194/acpd-9-20631-2009
- 784 Jensen, E. J., van den Heever, S. C., & Grant, L. D. (2018). The lifecycles of ice
 785 crystals detrained from the tops of deep convection. *Journal of Geophys-
 786 ical Research: Atmospheres*, 1–11. Retrieved from [http://doi.wiley.com/
 787 10.1029/2018JD028832](http://doi.wiley.com/10.1029/2018JD028832) doi: 10.1029/2018JD028832
- 788 Kato, S., Rose, F. G., Sun-Mack, S., Miller, W. F., Chen, Y., Rutan, D. A., ...
 789 Collins, W. D. (2011). Improvements of top-of-atmosphere and surface irra-
 790 diance computations with CALIPSO-, CloudSat-, and MODIS-derived cloud
 791 and aerosol properties. *Journal of Geophysical Research Atmospheres*, 116(19),
 792 1–21. doi: 10.1029/2011JD016050

- 793 Khairoutdinov, M. F., Krueger, S. K., Moeng, C.-H., Bogenschutz, P. A., & Ran-
794 dall, D. A. (2009). Large-eddy simulation of maritime deep tropical con-
795 vection. *Journal of Advances in Modeling Earth Systems*, *1*(15), 13. doi:
796 10.3894/james.2009.1.15
- 797 Khairoutdinov, M. F., & Randall, D. A. (2003). Cloud Resolving Model-
798 ing of the ARM Summer 1997 IOP : Model Formulation , Results , Un-
799 certainties , and Sensitivities. *Journal of the Atmospheric Sciences*,
800 *60*, 607–625. Retrieved from [http://journals.ametsoc.org/doi/
801 pdf/10.1175/1520-0469\(2003\)060%3C0607:CRMOTA%3E2.0.CO;2](http://journals.ametsoc.org/doi/pdf/10.1175/1520-0469(2003)060%3C0607:CRMOTA%3E2.0.CO;2) doi:
802 10.1175/1520-0469(2003)060(0607:CRMOTA)2.0.CO;2
- 803 Krämer, M., Rolf, C., Luebke, A., Afchine, A., Spelten, N., Costa, A., ... Aval-
804 lone, L. (2016). A microphysics guide to cirrus clouds Part 1: Cirrus
805 types. *Atmospheric Chemistry and Physics*, *16*(21), 3463–3483. Retrieved
806 from <http://www.atmos-chem-phys-discuss.net/15/31537/2015/> doi:
807 10.5194/acpd-15-31537-2015
- 808 Lilly, D. K. (1988). Cirrus outflow dynamics. *J. Atmos. Sci.*, *45*(10).
- 809 Liu, C., Shige, S., Takayabu, Y. N., & Zipser, E. (2015). Latent heating contribution
810 from precipitation systems with different sizes, depths, and intensities in the
811 tropics. *Journal of Climate*, *28*(1), 186–203. doi: 10.1175/JCLI-D-14-00370.1
- 812 Liu, X., & Penner, J. E. (2005). Ice nucleation parameterization for global
813 models. *Meteorologische Zeitschrift*, *14*(4), 499–514. Retrieved from
814 [http://openurl.ingenta.com/content/xref?genre=article&issn=0941
815 -2948&volume=14&issue=4&spage=499](http://openurl.ingenta.com/content/xref?genre=article&issn=0941-2948&volume=14&issue=4&spage=499) doi: 10.1127/0941-2948/2005/0059
- 816 Lohmann, U., & Roeckner, E. (1995). Influence of cirrus cloud radiative forcing on
817 climate and climate sensitivity in a general circulation model. *Journal of Geo-
818 physical Research*, *100*(D8), 16305. Retrieved from [http://doi.wiley.com/10
819 .1029/95JD01383](http://doi.wiley.com/10.1029/95JD01383) doi: 10.1029/95JD01383
- 820 Luo, Z., & Rossow, W. B. (2004). Characterizing Tropical Cirrus Life Cycle, Evolu-
821 tion, and Interaction with Upper-Tropospheric Water Vapor Using Lagrangian
822 Trajectory Analysis of Satellite Observations. *Journal of Climate*, *17*, 4541–
823 4563. Retrieved from [http://journals.ametsoc.org/doi/pdf/10.1175/
824 3222.1](http://journals.ametsoc.org/doi/pdf/10.1175/3222.1) doi: 10.1175/3222.1
- 825 Martins, E., Noel, V., & Chepfer, H. (2011). Properties of cirrus and subvisi-
826 ble cirrus from nighttime Cloud-Aerosol Lidar with Orthogonal Polarization
827 (CALIOP), related to atmospheric dynamics and water vapor. *Journal of Geo-
828 physical Research*, *116*(D2), D02208. Retrieved from [http://doi.wiley.com/
829 10.1029/2010JD014519](http://doi.wiley.com/10.1029/2010JD014519) doi: 10.1029/2010JD014519
- 830 Massie, S., Gettelman, A., Randel, W., & Baumgardner, D. (2002). Distribution
831 of tropical cirrus in relation to convection. *Journal of Geophysical Research At-
832 mospheres*, *107*(21), 1–16. doi: 10.1029/2001JD001293
- 833 Mauritsen, T., & Stevens, B. (2015). Missing iris effect as a possible cause of muted
834 hydrological change and high climate sensitivity in models. *Nature Geoscience*,
835 *8*(5), 346–351. Retrieved from [http://www.nature.com/doi/finder/10.1038/
836 ngeo2414](http://www.nature.com/doi/finder/10.1038/ngeo2414) doi: 10.1038/ngeo2414
- 837 Mlawer, E. J., Taubman, J., Brown, P. D., Iacono, M. J., & Clough, S. A. (1997).
838 Radiative transfer for inhomogeneous atmospheres: RRTM, a validated corre-
839 latedk model for the longwave. *Journal of Geophysical Research*, *102*(D14),
840 16663–16682. doi: doi:10.1029/97JD00237
- 841 Möhler, O., Field, P. R., Connolly, P., Benz, S., Saathoff, H., Schnaiter, M., ...
842 Karlsruhe, F. (2006). Efficiency of the deposition mode ice nucleation on
843 mineral dust particles. *Atmos. Chem. Phys.*, *6*, 3007–3021.
- 844 Morrison, H., Curry, J. A., & Khvorostyanov, V. I. (2005). A New Double-Moment
845 Microphysics Parameterization for Application in Cloud and Climate Models.
846 Part I: Description. *Journal of the Atmospheric Sciences*, *62*(6), 1665–1677.
847 Retrieved from <http://journals.ametsoc.org/doi/abs/10.1175/JAS3446.1>

- 848 doi: 10.1175/JAS3446.1
- 849 Morrison, H., & Milbrandt, J. A. (2015). Parameterization of Cloud Microphysics
850 Based on the Prediction of Bulk Ice Particle Properties. Part I: Scheme De-
851 scription and Idealized Tests. *Journal of the Atmospheric Sciences*, *72*(1),
852 287–311. Retrieved from [http://journals.ametsoc.org/doi/10.1175/
853 JAS-D-14-0065.1](http://journals.ametsoc.org/doi/10.1175/JAS-D-14-0065.1) doi: 10.1175/JAS-D-14-0065.1
- 854 Powell, S. W., Houze, R. A. J., Kumar, A., & McFarlane, S. A. (2012). Compari-
855 son of Simulated and Observed Continental Tropical Anvil Clouds and Their
856 Radiative Heating Profiles. *Journal of the Atmospheric Sciences*, *69*(9), 2662–
857 2681. doi: 10.1175/jas-d-11-0251.1
- 858 Protat, A., Delanoë, J., O’Connor, E. J., & L’Ecuyer, T. S. (2010). The evaluation
859 of CloudSat and CALIPSO ice microphysical products using ground-based
860 cloud radar and lidar observations. *Journal of Atmospheric and Oceanic Tech-
861 nology*, *27*(5), 793–810. doi: 10.1175/2009JTECHA1397.1
- 862 Protat, A., McFarquhar, G. M., Um, J., & Delanoë, J. (2011). Obtaining best esti-
863 mates for the microphysical and radiative properties of tropical ice clouds from
864 TWP-ICE in situ microphysical observations. *Journal of Applied Meteorology
865 and Climatology*, *50*(4), 895–915. doi: 10.1175/2010JAMC2401.1
- 866 Protopapadaki, S. E., Stubenrauch, C. J., & Feofilov, A. G. (2017). Upper Tropo-
867 spheric Cloud Systems Derived from IR Sounders: Properties of Cirrus
868 Anvils in the Tropics. *Atmospheric Chemistry and Physics*, *17*, 3845–
869 3859. Retrieved from www.atmos-chem-phys.net/17/3845/2017/ doi:
870 10.5194/acp-17-3845-2017
- 871 Ramanathan, V., Cess, R. D., Harrison, E. F., Minnis, P., Barkstrom, B. R., Ah-
872 mad, E., & Hartmann, D. L. (1989). Cloud-Radiative Forcing and Climate
873 : Results from the Earth Radiation Budget Experiment Linked references are
874 available on JSTOR for this article : Cloud-Radiative Forcing and Climate
875 : Results from the Earth Radiation Budget Experiment. *Science*, *243*(4887),
876 57–63.
- 877 Ramanathan, V., & Collins, W. (1991). Thermodynamic regulation of ocean warm-
878 ing by cirrus clouds deduced from observations of the 1987 El Niño. *Nature*,
879 *351*(6321), 27–32. doi: 10.1038/351027a0
- 880 Riihimaki, L. D., McFarlane, S. A., Liang, C., Massie, S. T., Beagley, N., & Toth,
881 T. D. (2012). Comparison of methods to determine Tropical Tropopause Layer
882 cirrus formation mechanisms. *Journal of Geophysical Research*, *117*(6), 1–14.
883 doi: 10.1029/2011JD016832
- 884 Ruppert, J. H., & Klocke, D. (2019). The two diurnal modes of tropical upward mo-
885 tion. *Geophysical Research Letters*. Retrieved from [http://doi.wiley.com/
886 10.1029/2018GL081806](http://doi.wiley.com/10.1029/2018GL081806) doi: 10.1029/2018GL081806
- 887 Sassen, K., Wang, Z., & Liu, D. (2009). Cirrus clouds and deep convection in
888 the tropics: Insights from CALIPSO and CloudSat. *Journal of Geophysical
889 Research: Atmospheres*, *114*(21), 1–11. doi: 10.1029/2009JD011916
- 890 Schmidt, C. T., & Garrett, T. J. (2013). A Simple Framework for the Dy-
891 namic Response of Cirrus Clouds to Local Diabatic Radiative Heating.
892 *Journal of the Atmospheric Sciences*, *70*(5), 1409–1422. Retrieved from
893 <http://journals.ametsoc.org/doi/abs/10.1175/JAS-D-12-056.1> doi:
894 10.1175/JAS-D-12-056.1
- 895 Schumacher, C., Houze, R. A. J., & Kraucunas, I. (2004). The Tropical Dy-
896 namical Response to Latent Heating Estimates Derived from the TRMM
897 Precipitation Radar. *Journal of the Atmospheric Sciences*, *61*(12), 1341–
898 1358. Retrieved from [http://journals.ametsoc.org/doi/abs/10.1175/
899 1520-0469\(2004\)061\(1341:TTDRTL\)2.O.CO;2](http://journals.ametsoc.org/doi/abs/10.1175/1520-0469%282004%29061%3C1341%3ATTDRTL%3E2.O.CO%3B2) doi: 10.1175/
900 1520-0469(2004)061(1341:TTDRTL)2.O.CO;2
- 901 Skamarock, W. C., Klemp, J. B., Dudhia, J., Gill, D. O., Barker, D. M., Wang, W.,
902 & Powers, J. G. (2008). *A description of the Advanced Research WRF version*

- 903 3. *NCAR Technical note -475+STR.*
 904 Sobel, A. H., & Bretherton, C. S. (2000). Modeling tropical precipitation in a single
 905 column. *Journal of Climate*, *13*(24), 4378–4392. doi: 10.1175/1520-0442(2000)
 906 013(4378:MTPIAS)2.0.CO;2
 907 Starr, D. O., & Cox, S. K. (1985). Cirrus Clouds. Part I: A Cirrus Cloud Model.
 908 *Journal of Atmospheric Sciences*, *42*(23), 2663–2681.
 909 Stephens, G. L., Vane, D. G., Tanelli, S., Im, E., Durden, S., Rokey, M., ... Marc-
 910 hand, R. (2008). CloudSat mission: Performance and early science after the
 911 first year of operation. *Journal of Geophysical Research Atmospheres*, *114*(8),
 912 1–18. doi: 10.1029/2008JD009982
 913 Thompson, G., Field, P. R., Rasmussen, R. M., & Hall, W. D. (2008). Explicit fore-
 914 casts of winter precipitation using an improved bulk microphysics scheme. Part
 915 II: Implementation of a new snow parameterization. *Monthly Weather Review*,
 916 *136*(12), 5095–5115. doi: 10.1175/2008MWR2387.1
 917 Van Dienenhoven, B., Fridlind, A. M., Cairns, B., Ackerman, A. S., & Yorks, J. E.
 918 (2016). Vertical variation of ice particle size in convective cloud tops. *Geophys-*
 919 *ical Research Letters*, *43*(9), 4586–4593. doi: 10.1002/2016GL068548
 920 Wall, C. J., & Hartmann, D. L. (2018). Balanced Cloud Radiative Effects Across
 921 a Range of Dynamical Conditions Over the Tropical West Pacific. *Geophysical*
 922 *Research Letters*, *5*, 490–498. doi: 10.1029/2018GL080046
 923 Wall, C. J., Hartmann, D. L., Thieman, M. M., Smith, W. L., & Minnis, P. (2018).
 924 The Life Cycle of Anvil Clouds and the Top-of-Atmosphere Radiation Bal-
 925 ance over the Tropical West Pacific. *Journal of Climate*, *31*(24), 10059–
 926 10080. Retrieved from [http://journals.ametsoc.org/doi/10.1175/](http://journals.ametsoc.org/doi/10.1175/JCLI-D-18-0154.1)
 927 [JCLI-D-18-0154.1](http://journals.ametsoc.org/doi/10.1175/JCLI-D-18-0154.1) doi: 10.1175/JCLI-D-18-0154.1
 928 Whiteway, J., Cook, C., Gallagher, M., Choullarton, T., Harries, J., Connolly, P.,
 929 ... Hacker, J. (2004). Anatomy of cirrus clouds: Results from the Emer-
 930 alid airborne campaigns. *Geophysical Research Letters*, *31*(24), 1–4. doi:
 931 10.1029/2004GL021201
 932 Wielicki, B. A., Barkstrom, B. R., Harrison, E. F., Lee, R. B., Smith, G. L., &
 933 Cooper, J. E. (1996). Clouds and the Earth’s Radiant Energy System
 934 (CERES): An Earth Observing System Experiment. *Bulletin of the American*
 935 *Meteorological Society*, *77*(5), 853–868. doi: 10.1175/1520-0477(1996)077(0853:
 936 CATERE)2.0.CO;2
 937 Winker, D. M., Pelon, J., Coakley, J. A., Ackerman, S. A., Charlson, R. J., Colarco,
 938 P. R., ... Wielicki, B. A. (2010). The Calipso Mission: A Global 3D View of
 939 Aerosols and Clouds. *Bulletin of the American Meteorological Society*, *91*(9),
 940 1211–1229. doi: 10.1175/2010BAMS3009.1
 941 Yoneyama, K., Zhang, C., & Long, C. N. (2013). Tracking Pulses of the Madden-Jul-
 942 ian Oscillation. *Bulletin of the American Meteorological Society*, *94*(12), 1871–
 943 1891. doi: 10.1175/bams-d-12-00157.1